THE JOURNAL OF PHYSICAL CHEMISTRY C

Article

pubs.acs.org/JPCC

Bioinspired High-Potential Porphyrin Photoanodes

Gary F. Moore,[†,§] Steven J. Konezny,[†] Hee-eun Song,[†] Rebecca L. Milot,[†] James D. Blakemore,[†] Minjoo L. Lee,*[,‡] Victor S. Batista,*[,†] Charles A. Schmuttenmaer,*[,†] Robert H. Crabtree,*[,†] and Gary W. Brudvig*[,†]

[†]Department of Chemistry, Yale University, P.O. Box 208107, New Haven, Connecticut 06520-8107, United States

[‡]School of Engineering and Applied Science, Yale University, P.O. Box 208267, New Haven Connecticut 06520-8267, United States

Supporting Information

ABSTRACT: We report a selection of high-potential porphyrin photoanodes (HPPPs) for use in photoelectrochemical cells (PECs). The anodes consist of bispentafluorophenyl free-base and metallo-porphyrin sensitizers bearing anchoring groups for attachment to metal-oxide surfaces including TiO_2 and SnO_2 nanoparticles. The term "high potential" refers to the relatively large and positive value of the electrochemical reduction potential for the bispentafluorophenyl porphyrin radical cation ($P^{\bullet+} + e^- \rightarrow P$) as compared with more conventional nonfluorinated analogues. Photoelectrochemical measurements demonstrate the sensitizers used in these HPPPs extend the absorption of the bare anode well into the visible region. Terahertz spectroscopic studies show the photoexcited dyes are capable of injecting electrons into the conduction band of an underlying metal-oxide with appropriate energetics. The reduction potentials of the resulting photogenerated porphyrin radical cations are relatively high (ranging from ~1.35 to 1.65 V vs NHE depending on the sensitizer). This is demonstrated by the ability of dye-sensitized solar cells, containing our HPPPs, to use the Br_3^-/Br^- redox couple as a regenerative electron mediator with superior performance in comparison to results obtained using the lower-potential I_3^-/I^- relay. Computational modeling of the structures and equivalent circuits assists in a molecular-based understanding of these systems. Further, the oxidation power of the porphyrin radical cations generated in these bioinspired constructs is similar to that found in the reaction centers of their natural counterpart (photosystem II); thus, HPPPs are promising as components in artificial systems for photochemical water spitting applications.

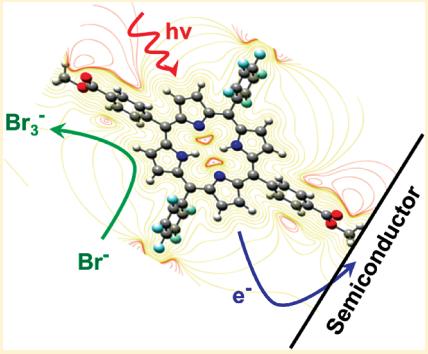

INTRODUCTION

The development of cost-effective alternative energy sources to meet global human energy demands (~16 TW) in an environmentally and socially responsible manner is critical to mitigating anthropogenic climate change and achieving energy security.[1−3] Of the available carbon-neutral energy sources, solar energy is abundant (striking the Earth's surface at a rate of ~120 000 TW), yet diffuse (~100 mW/cm^2) and intermittent.[4,5] Thus, devising low-cost methods for its capture, conversion, and storage is among the grand challenges of science.[6,7] Biological photosynthetic energy conversion offers many useful clues[8−10] that have prompted advances in the field of artificial photosynthesis.[4,11−18] In addition, sensitization of metal-oxide wide band gap semiconductor surfaces with inorganic transition-metal complexes or organic dyes has been actively pursued in developing methods for converting solar energy to electricity by dye-sensitized solar cells (DSSCs).[19−29] Such approaches typically rely on the use of relatively low potential regenerative mediators, (the I_3^-/I^- redox couple occurs at ~ +0.53 V vs NHE)[30] and in most cases do not adequately address the energetic requirements of water oxidation.

The first photoassisted water oxidation by Fujishima and Honda[31] produced hydrogen and oxygen from UV irradiation of n-type TiO_2. However, low quantum yields and limited use of the available solar energy spectrum are features not suitable for large-scale deployment. Examples of photoassisted and photoinduced water splitting have been reported using visible and visible coupled with ultraviolet light, respectively.[32−34] These systems incorporate a hybrid Ru−polypyridyl dye-sensitized Fujishima−Honda cell interfaced with a water-oxidation catalyst. In general, slow electron-transfer kinetics between the catalyst and photooxidized sensitizer, as well as fast back electron transfer from TiO_2, limit the quantum and energy storage efficiencies of these cells, detracting from their practicality. However, an increase of the driving force for electron transfer between the catalyst and photooxidized sensitizer might mitigate these overall unfavorable electron-transfer kinetics.[35]

In biological photosynthesis, the evolution of what became the water-oxidizing enzyme photosystem II (PSII) most likely

Received: October 20, 2011
Revised: January 20, 2012
Published: January 23, 2012

occurred via intermediate stages.[36,37] Early forms presumably operated on substrates that are easier to oxidize, and later forms, having more oxidizing reaction centers, became capable of water oxidation. Similar strategies may prove useful in developing artificial photosynthetic systems, most notably the development of light absorbers with potentials suitable for efficient water-oxidation chemistry. Porphyrins are a promising class of compounds in this regard as their electronic and optical properties are readily controlled via synthetic manipulation. This class of compounds has also shown recent promise as sensitizers in solar-to-electric application.[26]

We have previously reported a codeposited TiO_2 photoanode for visible light water splitting that utilizes a zinc porphyrin and an iridium water-oxidation catalyst.[38] Here, we report the optical and electronic properties for a selection of anodes sensitized with electron-deficient chromophores including the free base (**1**), zinc (**2**), and palladium (**3**) derivatives of a bispentafluorophenyl porphyrin bearing a carboxylate group for functionalization of metal-oxide surfaces including TiO_2 and SnO_2 nanoparticles (Chart 1). Investigation of these constructs via terahertz spectroscopy and photoelectrochemical measurements demonstrates the need for appropriately balancing the electronic and optical properties of the high potential dye and metal oxide.

Chart 1. Compounds 1−3

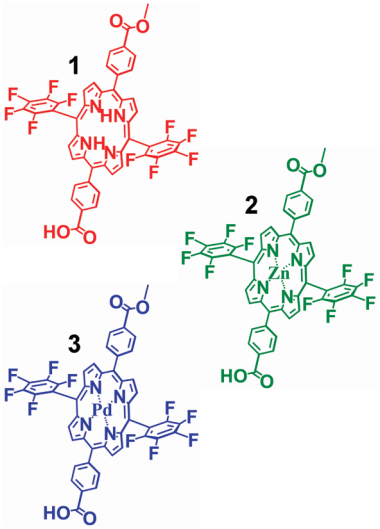

In this report, we aim to exploit the relative ease of assembly and testing of DSSCs as a platform for evaluating the energetics of dye/metal oxide interfaces, while screening for systems capable of oxidizing relatively high-potential sources of electrons and are, thus, promising candidates for developing water-oxidizing photoanodes. The Br_3^-/Br^- relay is ~500 mV more positive than the I_3^-/I^- couple;[39,40] thus, most sensitizers are insufficiently oxidizing to accept electrons from Br^-. Likewise, PECs that benefit from an increase in open-circuit voltage (V_{OC}) upon replacement of I_3^-/I^- by Br_3^-/Br^- are typically offset by a decrease in the short-circuit current (J_{SC}).[41−45]

EXPERIMENTAL SECTION

Sample Preparation and Characterization. All compounds were synthesized from commercially available starting materials (see Supporting Information, Synthesis and Structural Characterization). All chemicals were purchased from Aldrich or Alfa Aesar. Solvents were obtained from Aldrich or Mallinckrodt. Dichloromethane was purified with a solvent purification system (Innovative Technologies, Inc.) using a 1 m column containing activated alumina. All solvents were stored over the appropriate molecular sieves prior to use. Thin-layer chromatography (TLC) was performed with silica gel coated glass plates from EMD Chemicals. Column chromatography was carried out using silica gel 60, 230−400 mesh from EMD Chemicals. NMR spectra were recorded on Bruker spectrometers operating at 400 or 500 MHz. NMR samples were prepared in deuteriochloroform or 1% deuteriopyridine in deuteriochloroform with tetramethylsilane as an internal reference for ^1H NMR and trichlorofluoromethane as an external reference for ^{19}F NMR. Mass spectra were obtained with a matrix-assisted laser desorption/ionization time-of-flight (MALDI-TOF) spectrometer. Steady-state absorbance spectra were measured on a Varian Cary 300 UV−visible spectrophotometer. Films of TiO_2 and SnO_2 nanoparticles were highly scattering so spectra were obtained in diffuse reflectance geometry using an integrating sphere. Steady-state fluorescence spectra were measured using a Shimadzu RF-5301PC spectrometer.

Solar Cell Fabrication and Characterization. DSSCs were prepared in a manner similar to that reported previously.[39] Commercially available P25 TiO_2 and SnO_2 nanoparticles were used as received from Degussa (now Evonik) and Alfa Aesar, respectively. Fluorine-doped tin oxide (FTO) conductive glasses (Tec 8, visible light transmittance 77%, Hartford Inc., USA) were rinsed with ethanol before use. Pastes composed of 1.0 g of TiO_2 or 1.1 g of SnO_2 in 2 mL of Milli-Q water were stirred overnight to obtain a homogeneous dispersion and then coated by the doctor-blade method onto the FTO glasses with an area of 0.15 cm^2 and thickness ~10 μm. The electrodes were dried at room temperature and sintered in air at 450 °C for 2 h with a ramp rate of 5 °C/min. The TiO_2 and SnO_2 electrodes were sensitized by soaking in a 0.3 mM solution of N719 dye in ethanol or 0.1 mM solution of porphyrin compounds **1**−**3** in 10% ethanol in dichloromethane overnight at room temperature. Following sensitization, the photoanodes were rinsed with 10% ethanol in dichloromethane solution and dried at room temperature.

Counter electrodes were prepared by coating an FTO glass slide with two drops of 0.01 M hexachloroplatinic acid (H_2PtCl_2) in ethanol and heating at 400 °C for 15 min. An electrolyte (A) consists of 0.6 M *tert*-butylammonium iodide, 0.05 M iodine, 0.1 M lithium iodide, and 0.5 M *tert*-butyl pyridine in a 50/50 (v/v) mixture of valeronitrile and acetonitrile. An electrolyte (B) is 0.6 M *tert*-butylammonium bromide, 0.05 M bromine, 0.1 M lithium bromide, and 0.5 M *tert*-butyl pyridine in a 50/50 (v/v) mixture of valeronitrile and acetonitrile. To assemble a DSSC, a dye-sensitized TiO_2 or SnO_2 photoanode and a counter electrode were sealed to make a sandwich-type cell by heating with 60 μm thick Thermoplast hot-melt sealing material (SX1170-60, Solaronix SA, Switzerland) as a spacer between the electrodes. The electrolyte solution was injected into the cell through one of two predrilled holes in the counter electrode, and then the holes were sealed with a piece of the Thermoplast material covered by a piece of aluminum foil. The DSSCs were kept at room temperature for 2 h before photocurrent−voltage ($I-V$) and incident photon-to-current efficiency (IPCE) measurements. The irradiation source for the $I-V$ measurement was a 300 W ozone-free xenon lamp equipped

with a 50% IR blocking filter (Newport, USA) to simulate solar light. The light intensity was 100 mW/cm^2. The current−voltage curves were obtained by measuring the photocurrent of the cells using a Keithley model 2400 digital source meter under an applied external potential scan. Measurement of the IPCE of all cells was performed using a PV Measurements Inc. Solar Cell Spectral Response Measurement System Model QEXY utilizing monochromatic light from a xenon arc lamp filtered by a dual-grating monochromator and individual filters to test the device. Calibration of the instrument was performed prior to use by using a silicon photodiode for the whole calibration range, between 300 and 1000 nm. Due to the relatively slow response times of dye-sensitized solar cells, calibration of the instrument and all subsequent measurements were performed with a chopping speed of 5 Hz.

Reflectance Measurements. UV−visible spectra were taken on a Varian Cary 3 spectrophotometer with an integrating sphere attachment. Thin films of different TiO_2 or SnO_2 samples were prepared by the doctor-blade method on microscope slides and subjected to thermal treatment at 450 °C for 2 h with a ramp rate of 5 °C/min. The thin films were then sensitized with N719 dye or porphyrin dyes by soaking in an ethanol solution overnight and dried at room temperature before collecting spectra. The same sensitized films were also used in terahertz studies.

Electrochemical Measurements. Cyclic voltammetry was performed with an EG&G Princeton Applied Research Model 273 potentiostat/galvanostat using a glassy carbon (3 mm diameter) or platinum disk (1.6 mm diameter) working electrode, a platinum counter electrode, and a silver wire pseudoreference electrode in a conventional three-electrode cell. Anhydrous dichloromethane was used as the solvent for electrochemical measurements. The supporting electrolyte was tetrabutylammonium hexafluorophosphate in dichloromethane, and the solution was deoxygenated by bubbling with nitrogen. The working electrode was cleaned between experiments by polishing with an alumina slurry, followed by solvent rinses. The concentration of the electroactive compound was ~3 × 10^{-3} M. The potential of the pseudoreference electrode was determined using the ferrocenium/ferrocene redox couple as an internal standard (with $E_{1/2}$ taken as 0.690 V vs NHE in dichloromethane). The voltammograms were recorded at a 100 mV s^{-1} scan rate. All potentials listed in this manuscript are referenced to the normal hydrogen electrode (NHE).

Time-Resolved Terahertz Spectroscopy Measurements. An amplified Ti:sapphire laser (Tsunami/Spitfire from Spectra Physics) generated 800 mW of pulsed near-IR light at a 1 kHz repetition rate. The pulse width was 100 fs, and the center wavelength was 800 nm. Roughly two-thirds of the power was frequency doubled and then filtered to produce 40 mW of 400 nm (3.10 eV) light for the pump beam. The remainder of the near-IR light was used to generate and detect terahertz radiation. Terahertz radiation was generated using optical rectification in a ZnTe(110) crystal and detected using free space electro-optic sampling in a second ZnTe(110) crystal. Terahertz data were taken at room temperature, and the average of two samples was taken for each data set. To analyze electron injection dynamics, the change in terahertz transmission was monitored as the time delay between the 400 nm pump pulse and the terahertz probe pulse was varied. Further information on the spectrometer and techniques can be found in the literature.[46−48]

Computational Structural Modeling. Binding of Br$^-$ and I$^-$ anions to bispentafluorophenyl free-base and metallo-porphyrin sensitizers, bearing linkers for attachment to metal-oxide surfaces, has been analyzed for minimum energy configurations obtained at the B3LYP/6-31G(d,p) level for H, C, O, N, F, Br, and LanL2DZ for Zn, Pd, and I. All calculations were done in solvent (dichloromethane), using the PCM solvent model as implemented in the program Gaussian 09.[49] The electrostatic potential for sensitizers **1**−**3** was computed using the Merz−Singh−Kollman scheme.[50,51]

Modeling Current−Voltage Characteristic Curves. Scheme 1 shows a schematic energy level diagram for the kinetics of interfacial electron transfer induced by illumination of the photoanode and competing back transfer mechanisms as well as an equivalent circuit used to model the photocurrent−voltage characteristics of the photoelectrochemical cells under DC conditions.[52,53] The output current density as a function of applied bias voltage V was computed as follows

Scheme 1. Charge Transfer Kinetics Diagram (Top) and Equivalent Circuit (Bottom) Used to Model the Solar Cell Current−Voltage Characteristics (M = Ti, Sn; X = Br, I)[a]

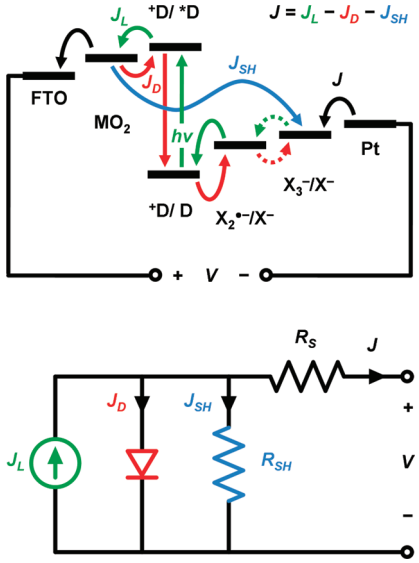

[a]The dominant mechanisms are shown including the current density J_L induced upon photoexcitation and electron injection into the conduction band of the semiconductor surface (green), recombination processes that behave as a diode (red) and a resistor (blue) in series with the current source, and a series resistance R_S that takes into account the resistances of the photoanode and electrolyte in solution.

$$J = J_L - J_D - J_{SH},$$
$$= J_L - J_0\left\{\exp\left[\frac{q(V + JAR_S)}{fkT}\right] - 1\right\} - \frac{V + JAR_S}{AR_{SH}} \quad (1)$$

where J_L is the illumination current density induced upon photexcitation and interfacial electron injection into the conduction band of the semiconductor surface; J_{SH} and R_{SH} are the shunt current density and resistance due to surface leakage caused by the direct recombination of the photoinjected carrier with redox species in the electrolyte solution and the dark current along the edges of the cell; and $J_D = J_0\{\exp[(q(V + JAR_S))/(fkT)] - 1\}$ is the current

dx.doi.org/10.1021/jp210096m | J. Phys. Chem. C 2012, 116, 4892−4902

density of the interfacial diode junction leading to recombination into the photooxidized dye. The latter contribution to the current density is modeled by the Shockley ideal diode equation for the net current flowing through the diode where J_0 is the saturation current which is the diode leakage current density in the absence of light; k is the Boltzmann's constant; T is the absolute temperature with kT/q = 0.0259 V; A is the device area; f is the ideality factor; and R_S is the cell series resistance including the bulk resistivity of the semiconductor and the resistance of the electrolyte. Equation 2 gives an estimate of the open circuit voltage of the cell with high shunt resistance

$$V_{OC} \approx \frac{f kT}{q} \ln\left(\frac{J_L}{J_0} + 1\right) \quad (2)$$

The sets of parameters that reproduce the experimental photocurrent–voltage characteristics via eq 1 for all devices studied are reported in Table 1.

RESULTS

Steady-State Optical Studies. To estimate the E^{0-0} transition energy of compounds **1**–**3**, we measured the steady-state absorption and emission spectra of methyl esters of these compounds (Figure 1). In dichloromethane, the absorption spectrum of the free base exhibits visible absorption peaks (Q bands) at 510, 543, 587, and 641 nm. In addition, an intense Soret band is present at 416 nm (see Supporting Information, Figures S1 and S2). Consistent with the rigid ring structure of the porphyrin, the emission spectrum of methyl ester of the free base (**1**) reveals a modest Stokes shift of 5 nm, with the shortest wavelength emission band at 646 nm. The intersection of the normalized absorption and emission spectra yields an estimated E^{0-0} transition energy of ~1.93 eV (see Supporting Information, Figure S3). In comparison, the longest-wavelength absorption and shortest-wavelength emission bands of the methyl ester of the zinc species (**2**) (λ_{max} = 578 and 590 nm, respectively) are of significantly higher energy relative to the associated free base analogue, yielding an estimated E^{0-0} transition energy of ~2.12 eV. For the methyl ester of the palladium species (**3**), the longest-wavelength absorption and shortest-wavelength emission bands are further blue-shifted (λ_{max} = 554 and 560 nm, respectively) in comparison with the related zinc analogue, yielding an

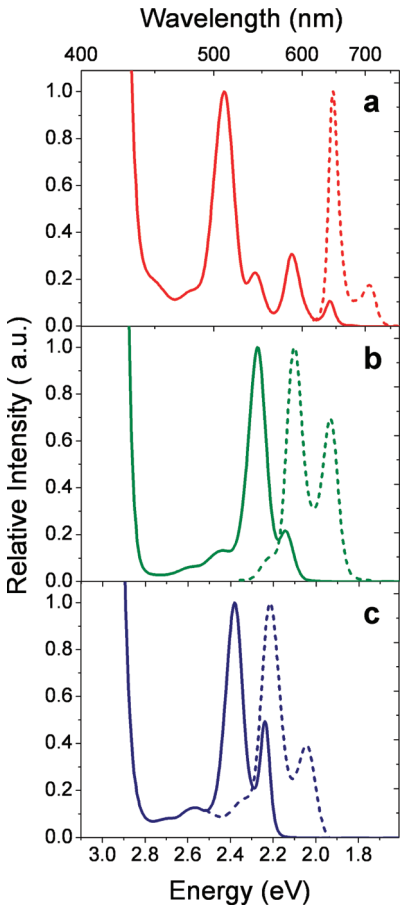

Figure 1. Absorption (solid lines) and emission (dashed lines) spectra of the methyl esters of (a) **1**, (b) **2**, and (c) **3** in dichloromethane.

Table 1. Performance of Solar Cells Based on 1, 2, 3, and N719 with Either I_3^-/I^- or Br_3^-/Br^- Redox Couples As Regenerative Electron Mediators and TiO_2 or SnO_2 Nanocrystalline Substrates Modeled by the Equivalent Circuit Shown in Scheme 1[a]

dye	oxide	electrolyte	J_L (mA/cm^2)	J_0 (mA/cm^2)	R_S (Ω)	R_{SH} (kΩ)	f
1	TiO_2	I_3^-/I^-	0.15	3.81×10^{-6}	46.0	27.4	1.72
		Br_3^-/Br^-	0.13	1.59×10^{-7}	195	46.4	2.23
	SnO_2	I_3^-/I^-	0.97	1.47×10^{-2}	47.2	12.3	3.18
		Br_3^-/Br^-	2.58	3.35×10^{-4}	778	97.9	2.81
2	TiO_2	I_3^-/I^-	0.93	4.20×10^{-6}	56.5	11.2	1.84
		Br_3^-/Br^-	0.17	9.47×10^{-7}	279	41.5	2.43
	SnO_2	I_3^-/I^-	2.83	4.82×10^{-6}	93.1	1.62	1.34
		Br_3^-/Br^-	1.35	1.16×10^{-6}	1377	247	1.62
3	TiO_2	I_3^-/I^-	0.26	2.15×10^{-3}	26.9	2.20	3.18
		Br_3^-/Br^-	0.17	5.46×10^{-9}	304	38.1	1.76
	SnO_2	I_3^-/I^-	0.76	1.85×10^{-2}	48.5	113	3.46
		Br_3^-/Br^-	3.48	3.13×10^{-5}	694	24.7	2.20
N719	TiO_2	I_3^-/I^-	9.62	5.53×10^{-3}	39.6	459	3.97
		Br_3^-/Br^-	0.16	7.09×10^{-5}	95.8	79.5	3.63
	SnO_2	I_3^-/I^-	11.1	3.26×10^{-2}	163	3.01	2.92
		Br_3^-/Br^-	0.25	6.95×10^{-5}	99.7	50.3	3.46

[a]Equivalent circuit parameters include the illumination and saturation current densities J_L and J_0, the series and shunt resistances R_S and R_{SH}, and the ideality factor f.

dx.doi.org/10.1021/jp210096m | J. Phys. Chem. C 2012, 116, 4892–4902

estimated E^{0-0} transition energy of ~2.23 eV. Although films of P25 TiO_2 nanoparticles sensitized with compounds **1**−**3** were highly scattering, spectra obtained in diffuse-reflectance geometry with an integrating sphere give the spectral profile of the sensitizing dye (see Supporting Information, Figure S4).

Electrochemical Studies. The 10,20-bis(pentafluorophenyl) groups have a strong influence on the electrochemical properties of the porphyrin ring system as the electron-withdrawing nature of these functional groups destabilizes the formation of the radical-cation species.[54] For the methyl ester derivative of the free base (**1**) in dichloromethane, two quasi-reversible one-electron redox processes are observed with midpoint potentials ($E_{1/2}$) of 1.57 and 1.78 V vs NHE (Figure 2).

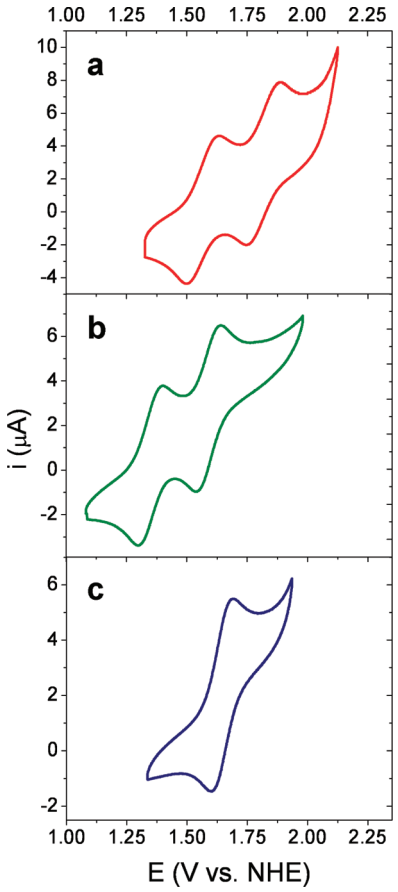

Figure 2. Cyclic voltammograms recorded at a glassy carbon electrode for the methyl-ester derivatives of (a) **1**, (b) **2**, and (c) **3** in dichloromethane.

These redox processes are significantly shifted in the anodic direction compared to the nonfluorinated analogue, 5,15-bis(4-carbomethoxyphenyl)-10,20-bis(2,4,5-trimethylphenyl)porphyrin, where the porphyrin radical cation/porphyrin redox couple occurs with an $E_{1/2}$ of 1.29 V vs NHE.[55] For the methyl ester of the zinc species (**2**), the first and second oxidations of the porphyrin occur with an $E_{1/2}$ of 1.35 and 1.59 V vs NHE, respectively, and are, thus, cathodically shifted versus the free base analogue. The electrochemical behavior of the methyl ester of the palladium species (**3**) differs from the zinc species. In this compound, the first oxidation is anodically shifted in comparison with the free base to an $E_{1/2}$ of 1.65 V vs NHE, but the second oxidation is obscured by limitations of the electrochemical window.

In accordance with the Rhem Weller approximation,[56,57] excited-state redox potentials for compounds **1**−**3** were estimated from the corresponding ground-state potentials and E^{0-0} transition energies as expressed in eq 3

$$E^{\circ}(P^{\bullet+}/{}^{1}P) \approx E^{\circ}(P^{\bullet+}/P) - \frac{E^{0-0}(P \rightarrow {}^{1}P)}{e} \quad (3)$$

where $E^{\circ}(P^{\bullet+}/{}^{1}P)$ is the excited-state potential for the porphyrin-radical cation/excited-singlet state porphyrin couple; $E^{\circ}(P^{\bullet+}/P)$ is the ground-state potential for the porphyrin-radical cation/porphyrin couple, $E^{0-0}(P \rightarrow {}^{1}P)$ is the estimated E^{0-0} porphyrin ground state to porphyrin excited-singlet state transition energy; and e is the elementary charge of an electron. The values of these excited-state potentials are pertinent, as they determine the thermodynamic feasibility of photoinduced electron transfer to the bound metal oxide, as expressed in eq 4

$$\Delta G^{\circ}_{ET} = eE^{\circ}(P^{\bullet+}/{}^{1}P) - eE^{\circ}_{CB} \quad (4)$$

where ΔG°_{ET} is the free energy of excited-state electron transfer and E°_{CB} denotes the metal-oxide conduction-band potential. Conversely, ground-state potentials allow for an estimation of the potential photogenerated at the anode surface, which in turn determines the driving force for hole transfer to a given electron donor, in this study I^- or Br^-, as expressed in eq 5

$$\Delta G^{\circ}_{HT} = eE^{\circ}(X_2^{\bullet-}/X^-) - eE^{\circ}(P^{\bullet+}/P) \quad (5)$$

where ΔG°_{HT} is the free energy of ground-state hole transfer, and $E^{\circ}(X_2^{\bullet-}/X^-)$ denotes the potential for the one electron dihalide radical anion/halide couple. Ultimately, the ground and excited state potentials are pinned together by the E^{0-0} transition energy of the material (Scheme 2). In a photoelectrochemical cell, a fraction of this energy can be converted to electrical potential, where the maximum obtainable V_{OC} depends on the quasi-Fermi level of the metal oxide conduction band and the redox potential of the solution. To facilitate comparison, estimated potentials, taken from the literature, for the TiO_2[58] and SnO_2[20] conduction bands, as well as the I_3^-/I^-[30] and Br_3^-/Br^-[40] redox couples, are included in Scheme 2 along with the estimated ground state and excited state potentials for compounds **1**−**3**. The precise values of these potentials are sensitive to the specific sensitizer and electrolyte conditions used. Likewise, experimental values obtained in the absence of some components of an operational cell may not reflect actual values. Because the Fermi level depends on the electron concentration in the metal oxide, changes in V_{OC} can be related to recombination processes as expressed in eq 6[59−61]

$$V_{OC} = \frac{kT}{e} \ln\left(\frac{J_{inj}}{k_{rec}\eta_{c,0}[I_3^-]}\right) \quad (6)$$

where J_{inj} is the flux of injected electrons; k_{rec} is the rate constant for I_3^- reduction; and $\eta_{c,0}$ is the conduction band electron density in the dark.

Time-Resolved Terahertz Studies. Interfacial electron transfer dynamics of functionalized metal-oxide nanoparticle thin films were studied, with subpicosecond temporal resolution, using time-resolved terahertz spectroscopy. In these experiments, terahertz radiation is absorbed by mobile electrons in the metal-oxide conduction band, and the change in terahertz amplitude is a product of the carrier density and mobility.[44] Photoexcitation and subsequent electron injection

Scheme 2. Energy Level Diagram Illustrating Reduction Potentials of Relevant Half Reactions[a]

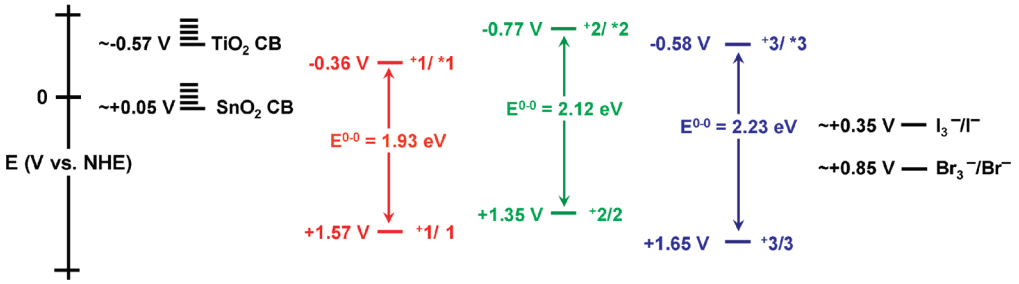

[a]Ground-state and excited-state potentials of porphyrins **1** (red), **2** (green), and **3** (blue) were determined by cyclic voltammetry measurements together with absorption and emission spectra. To facilitate comparison, approximate potentials for the TiO_2[56] and SnO_2[20] conduction bands, as well as the I_3^-/I^-[30] and Br_3^-/Br^-[38] couples, are also included. Note the O_2/H_2O couple is 0.82 V at pH = 7, and all potentials are reported in V vs NHE.

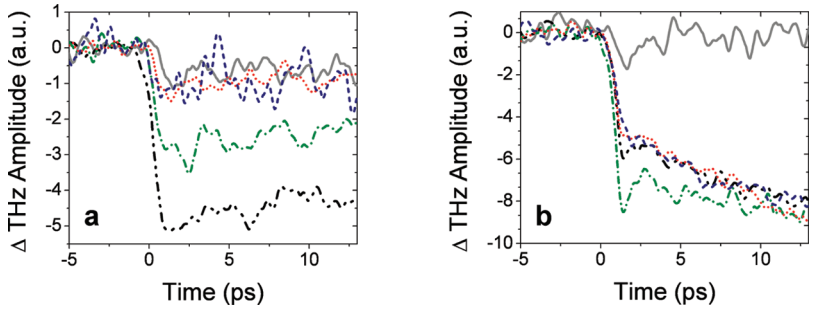

Figure 3. 400 nm pump/terahertz probe of electron injection of (a) TiO_2 and (b) SnO_2 nanoparticle thin films, including bare films (gray) and films functionalized with the following: **1** (red dot), **2** (green dash-dot), **3** (blue dash), and N719 (black dash-dot-dot).

result in an increase of the metal-oxide free-carrier population, decreasing the terahertz transmission amplitude. Thus, such measurements allow for a direct comparison of the time scale and efficiency of photoinduced charge injection and recombination or trapping.

Results obtained for the 400 nm optical pump/terahertz probe of TiO_2 and SnO_2 nanoparticle thin films, including bare films and films functionalized with compounds **1**−**3** and N719, are illustrated in Figure 3. Indeed, there is a negligible change in the terahertz transmittance of the bare TiO_2 and SnO_2 samples, consistent with the negligible absorbance at 400 nm for these metal oxides. Results, obtained using N719 as the sensitizing dye, indicate effective photoinduced charge injection on both TiO_2 and SnO_2 films. By contrast, only the zinc derivative (**2**) of compounds **1**−**3** gives rise to any significant terahertz absorption on both TiO_2 and SnO_2. For the more highly oxidizing free base and palladium derivatives, only the SnO_2 films give rise to effective charge injection. These results are consistent with the excited-state potentials listed in Scheme 2 and the more positive potential of the SnO_2 conduction band in comparison with TiO_2.

Although the excited-state potential of the Pd derivative (**3**) is estimated to be slightly negative of the TiO_2 conduction band, no appreciable change in terahertz amplitude is detected in these systems, suggesting that deactivation pathways other than interfacial charge transfer dominate. For Pd porphyrins, rapid intersystem crossing (ISC) to the triplet state due to increased spin orbit coupling induced by the heavy atom effect of palladium may be involved. The potential of the triplet state is most likely poised positive of the TiO_2 conduction band. However, no attempts were made in this study to elucidate the mechanism of possible competing deactivation pathways.

Also evident in Figure 3 are the differing time scales of electron injection for all of the sensitizing dyes attached to SnO_2 versus TiO_2. These distinctions have been reported in the literature for Ru polypyridyl sensitizing dyes, and our observations are consistent with those studies.[62−65] For TiO_2, electron injection is completed within the instrument response-limited time of approximately 300 fs after photoexcitation for all of the dyes studied. Injection into SnO_2 is slower and is biphasic with an injection component which is completed within the instrument response-limited time and a slower component which continues for 10−80 ps.

Photocurrent−Voltage Characteristics of Nanocrystalline Photoelectrochemical Cells. DSSC photoanodes composed of either TiO_2 or SnO_2 nanoparticles sensitized with compounds **1**−**3**, as well as N719, were prepared using the I_3^-/I^- or Br_3^-/Br^- couple as a regenerative electron mediator and a Pt counter electrode as the cathode (see Experimental Section for details). In these constructs, the maximum obtainable V_{OC} depends on the quasi-Fermi level of the metal oxide conduction band and the redox potential of the solution. To allow for a fairer comparison of performance between cells made with TiO_2 versus SnO_2, no attempts were made to improve the overall cell efficiency by adopting techniques such as surface treatment of TiO_2 films with $TiCl_4$. For DSSCs, the overall energy conversion efficiency (η), is a product of the short-circuit current density (J_{SC}), the open-circuit voltage (V_{OC}), and the fill factor (FF) according to eq 7

$$\eta = \frac{\text{power out}}{\text{power in}} = \frac{V_{OC} \times J_{SC} \times FF}{P_{in}} \quad (7)$$

where P_{in} is the total solar incident on the cell (100 mW/cm^2 for AM 1.5). The measured photovoltaic parameters are summarized in Table 2.

dx.doi.org/10.1021/jp210096m | J. Phys. Chem. C 2012, 116, 4892−4902

Table 2. Photovoltaic Parameters, Including the Open Circuit Voltage V_{OC}, Short-Circuit Current Density J_{SC}, Fill Factor FF, and Efficiency η Measured at 100 mW/cm^2 Illumination

dye	oxide	electrolyte	J_{SC} (mA/cm^2)	V_{OC} (V)	FF	η
1	TiO_2	A (I_3^-/I^-)	0.14	0.37	0.31	0.02
		B (Br_3^-/Br^-)	0.13	0.62	0.26	0.02
	SnO_2	A (I_3^-/I^-)	1.01	0.31	0.32	0.10
		B (Br_3^-/Br^-)	2.53	0.64	0.47	0.76
2	TiO_2	A (I_3^-/I^-)	0.90	0.55	0.51	0.25
		B (Br_3^-/Br^-)	0.21	0.69	0.42	0.06
	SnO_2	A (I_3^-/I^-)	2.51	0.37	0.41	0.39
		B (Br_3^-/Br^-)	1.32	0.59	0.51	0.40
3	TiO_2	A (I_3^-/I^-)	0.25	0.37	0.26	0.02
		B (Br_3^-/Br^-)	0.16	0.62	0.3	0.03
	SnO_2	A (I_3^-/I^-)	0.81	0.31	0.37	0.09
		B (Br_3^-/Br^-)	3.37	0.66	0.45	1.00
N719	TiO_2	A (I_3^-/I^-)	9.59	0.77	0.61	4.48
		B (Br_3^-/Br^-)	0.15	0.67	0.45	0.05
	SnO_2	A (I_3^-/I^-)	10.33	0.46	0.38	1.82
		B (Br_3^-/Br^-)	0.04	0.08	0.71	0.00

TiO_2 Anodes Using the I_3^-/I^- Mediator. For anodes composed of TiO_2 using the I_3^-/I^- mediator—conditions employed in a typical Grätzel-type DSSC—only a negligible photocurrent is obtained with compounds **1** and **3** as sensitizer (Figure 4(a) and Table 2). These results, obtained in complete photoelectrochemical cells, are consistent with terahertz data performed on isolated dye-sensitized thin films. Thus, such poor performance is most likely due to unfavorable energetic positioning of the excited state of these relatively highly oxidizing dyes in comparison with the more negative conduction band of TiO_2 versus SnO_2 (Scheme 2). For similar cells, sensitized with compound **2**, a modest photocurrent (0.9 mA/cm^2) is obtained at short circuit, consistent with the conclusion that the excited state relay of **2** is poised negative of the TiO_2 conduction band. For comparison, results obtained using a similar cell configuration but with TiO_2, I_3^-/I^-, and N719 are illustrated in Figure 5(a) and Table 2. It is clear that cells with N719 are far superior in overall performance versus cells employing porphyrin dyes (**1**–**3**) studied here on TiO_2 with I_3^-/I^- (Table 2).

TiO_2 Anodes Using the Br_3^-/Br^- Mediator. In this case, only a negligible photocurrent is obtained with **1** and **3** as sensitizers (Figure 4(a) and Table 2), consistent with the unfavorable energetic positioning of the excited state of these chromophores with respect to the TiO_2 conduction band (Scheme 2). However, cells sensitized with compound **2**, where the potential of the excited-state dye should be poised negative of the TiO_2 conduction band, show an overall diminished performance in comparison with the measurements obtained using the I_3^-/I^- mediator and TiO_2 as the metal oxide (a 76% decrease in η) (Figure 4(a) and Table 2). These results indicate comparatively unfavorable thermodynamic and kinetic electron transfer characteristics for cells utilizing this relatively lower-potential (in comparison with compounds **1** and **3**) porphyrin dye upon replacing the I_3^-/I^- mediator with Br_3^-/Br^-. For comparison, results obtained using a similar cell configuration with TiO_2, Br_3^-/Br^-, and N719 are illustrated in Figure 5(a) and Table 2. It is clear that the overall cell performance is drastically

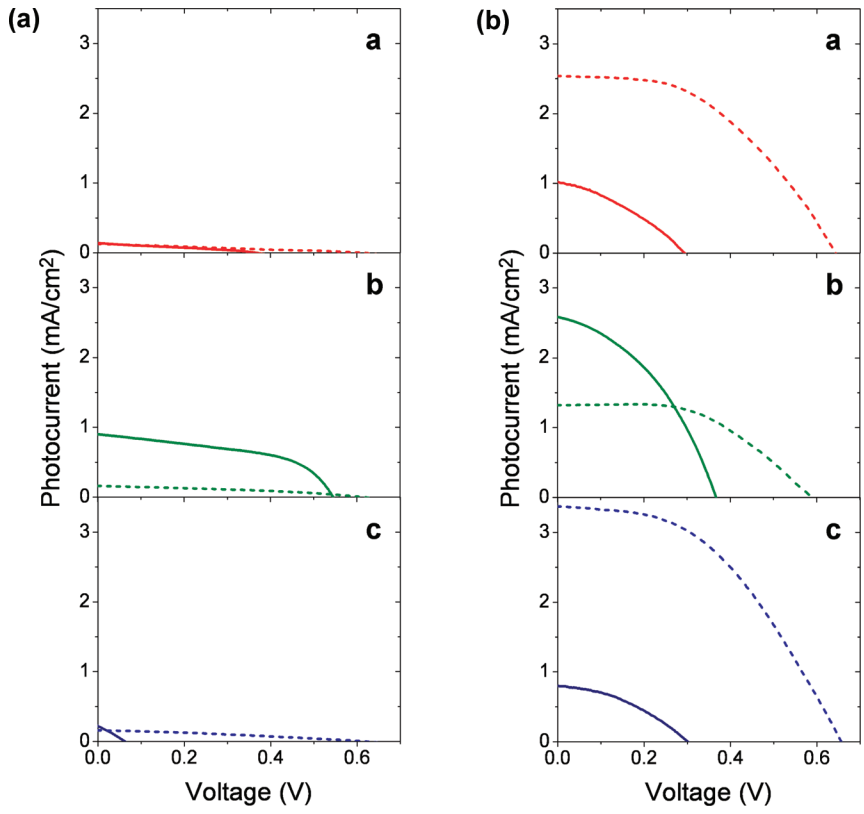

Figure 4. (a) Photocurrent–voltage characteristics of TiO_2 nanocrystalline photoelectrochemical cells sensitized with (a) **1**, (b) **2**, and (c) **3** using either the I_3^-/I^- (solid lines) or Br_3^-/Br^- (dashed lines) redox couple as a regenerative electron mediator. (b) Photocurrent–voltage characteristics of SnO_2 nanocrystalline photoelectrochemical cells sensitized with (a) **1**, (b) **2**, and (c) **3** using either the I_3^-/I^- (solid lines) or Br_3^-/Br^- (dashed lines) redox couple as a regenerative electron mediator.

dx.doi.org/10.1021/jp210096m | J. Phys. Chem. C 2012, 116, 4892–4902

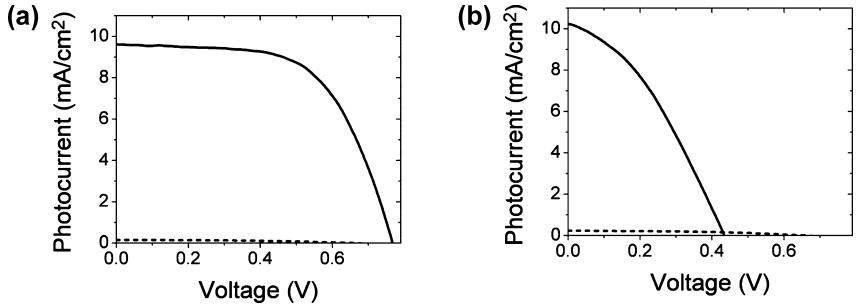

Figure 5. (a) Photocurrent−voltage characteristics of TiO_2 nanocrystalline photoelectrochemical cells sensitized with N719 using either the I_3^-/I^- (solid lines) or Br_3^-/Br^- (dashed line) redox couple as a regenerative electron mediator. (b) Photocurrent−voltage characteristics of SnO_2 nanocrystalline photoelectrochemical cells sensitized with N719 using either the I_3^-/I^- (solid lines) or Br_3^-/Br^- (dashed line) redox couple as a regenerative electron mediator.

diminished upon replacing the I_3^-/I^- mediator with Br_3^-/Br^- (a 99% decrease in η), reflecting the inability of this dye (N719) to effectively utilize the higher-potential Br_3^-/Br^- couple.

SnO_2 Anodes Using the I_3^-/I^- Mediator. Moving from TiO_2 to the more positively poised SnO_2 has a significant effect on cell performance with sensitizers **1**−**3**. This change results in a 400%, 56%, and 350% increase in η, respectively, in comparison with the I_3^-/I^- mediator and TiO_2 as the metal oxide (Figure 4(b) and Table 2). Although all the porphyrin-based anodes show an increase in J_{SC} upon substituting Sn for Ti with I_3^-/I^- as the redox mediator, the V_{OC} is limited by the positive energetic displacement of the SnO_2 conduction band with respect to TiO_2. These are, however, the same energetic conditions which favor initial photoinduced charge separation in these HPPPs. By comparison, cells with N719 show a V_{OC} comparable to those obtained in the porphyrin systems under similar conditions (Figure 5(b) and Table 2). However, for cells sensitized with N719, the overall energy conversion efficiency is decreased upon replacing TiO_2 with SnO_2 as semiconductor. We see a 59% decrease in η in comparison with the I_3^-/I^- mediator and TiO_2 as the metal oxide. This decrease in η is due to the decreased V_{OC} and the relatively poor fill factor (FF) associated with SnO_2. This represents a 40% and 38% decrease in V_{OC} and FF, respectively, in comparison with measurements obtained using the I_3^-/I^- mediator and TiO_2 as the metal oxide.

SnO_2 Anodes Using the Br_3^-/Br^- Mediator. The overall lower V_{OC} obtained with SnO_2 versus TiO_2 could be improved if the photoxidized dye was capable of efficiently turning over a higher-potential redox mediator such as the Br_3^-/Br^- couple. This is indeed the case for cells using compounds **1** and **3** as sensitizer where there is an overall increase in both V_{OC} and J_{SC}, resulting in a 660% and 1011% increase in η, respectively, in comparison with the measurements obtained for I_3^-/I^- and SnO_2 (Figure 4(b) and Table 2). For the lower-potential species **2**, the increase in V_{OC} obtained with Br_3^-/Br^- comes at the expense of a decrease of J_{SC}, resulting in a 3% increase in η compared with using I_3^-/I^- as mediator and SnO_2 as the metal oxide. For cells sensitized with N719, the inability of this dye to effectively utilize the higher-potential Br_3^-/Br^- couple as redox mediator results in zero photocurrent under these cell conditions (Figure 5(b) and Table 2). Thus, the high-potential dyes **1** and **3** are most efficient under the same conditions in which the lower-potential N719 is most inefficient, i.e., with SnO_2 as the metal oxide and Br_3^-/Br^- as the mediator. Conversely, the high-potential dyes **1** and **3** are most inefficient under the same conditions in which the lower-potential N719 is most efficient, i.e., with TiO_2 as the metal oxide and I_3^-/I^- as the mediator). These results illustrate the critical interplay between the various components of these molecular photoelectrochemical devices and the need to appropriately balance their electronic and optical properties upon displacing the energetics of the overall system to more oxidizing conditions.

Photocurrent Action Spectra Obtained with Nanocrystalline Photoelectrochemical Cells. For DSSCs, external quantum efficiency of a given system is typically reported in terms of incident photon to current efficiency (IPCE). As expressed in eq 8

$$\mathrm{IPCE} = \mathrm{LHE} \times \phi_{\mathrm{inj}} \times \eta_{\mathrm{C}} \tag{8}$$

IPCE is the product of the light harvesting efficiency (LHE) of the dye at a given wavelength, the electron injection efficiency (Φ_{inj}), and the charge collection efficiency (η_C). Thus, IPCE action spectra offer insight into the efficiency of photoelectric conversion as a function of excitation wavelength. Likewise, the IPCE should reflect the spectral profile of the sensitizing dye (Figure 6). However, the immobilized species are red-shifted in comparison with solution absorption measurements of the model methyl ester compounds, indicating a coupling of the transition moments of the dyes with the surface.

Analysis of Current Voltage Curves. The performance of solar cells based on sensitizers **1**, **2**, **3**, and N719, using either I_3^-/I^- or Br_3^-/Br^- redox couples as regenerative electron mediators and TiO_2 or SnO_2 nanocrystalline substrates, is reported in Tables 1 and 2. These results show an increase in the series resistance by a factor of between 1 and 4 when the TiO_2 photoanode is replaced by SnO_2 for a given dye and electrolyte reflecting a higher conductivity in the TiO_2 photoanodes. R_S increases by a factor of between 4 and 17 for bromide relative to iodide for dyes **1**−**3**, consistent with higher conductivities reported for iodide over bromide at low concentrations.[44] A more significant impact of the substitution of I^- by Br^- on the current−voltage characteristics for solar cells based on sensitizers **1**−**3** is the systematic reduction of the saturation recombination current J_0 and increase in the open circuit voltage V_{OC}. This trend can be understood based on electrostatic potential calculations that show tighter binding of bromide to the porphyrins.

The computed electrostatic potential (see Supporting Information) shows evidence of stabilization of the Br^- redox species by polarization and electrostatic contributions, including the interaction of the anions with the permanent quadrupole moments of the aromatic rings.[66,67] With its

dx.doi.org/10.1021/jp210096m | J. Phys. Chem. C 2012, 116, 4892−4902

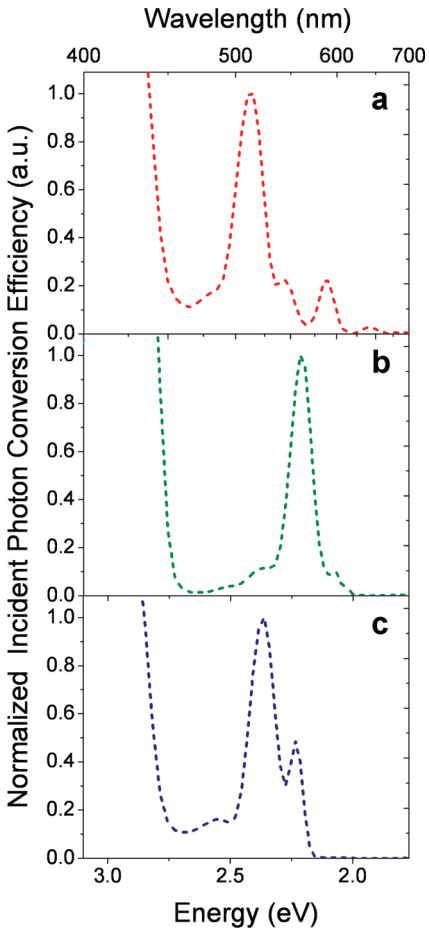

Figure 6. Normalized photocurrent action spectra obtained with SnO_2 nanocrystalline photoelectrochemical cells sensitized with (a) **1**, (b) **2**, and (c) **3** using the Br_3^-/Br^- redox couple as a regenerative electron mediator.

smaller ionic radius (Br^-: 1.82 Å, I^-: 2.06 Å), Br^- interacts more strongly and binds more closely to the aromatic rings than I^- by anion-π stabilization. Up to four Br^- anions per porphyrin are predicted to bind to **1** and **3** with a stabilization energy between −5 and −13 kcal/mol, including two Br^- ions bound to the pentafluorophenyl groups and two additional Br^- ions bound to the carbomethoxyphenyl groups (see Figure 7 and Table 3). We also find that one additional Br^- binds to the Zn center of **2** with the substantial stabilization energy of −12.5 kcal/mol. This is a much stronger metal−anion interaction than seen for Zn−I^- and Pd−Br^- where the corresponding stabilization energies are very low: less negative than −1.0 kcal/mol. This can be attributed to both the relative size of studied anions and a more favorable charge distribution for anion binding in **2** than the other compounds (see Supporting Information). In contrast to the studies with bromide, calculations of the interactions between **1**−**3** and the larger iodide ions show negligible or no stabilization due to ion binding.

The electrostatic field of anions in the solution shifts the electron donor and acceptor states, as well as the edge of the conduction band, to more negative potentials and reduces the concentration of electrons at the surface. The larger stabilization energy of the closely bound bromide ions leads to a larger shift toward negative potentials in the donor state relative to the bottom of the semiconductor conduction band, which

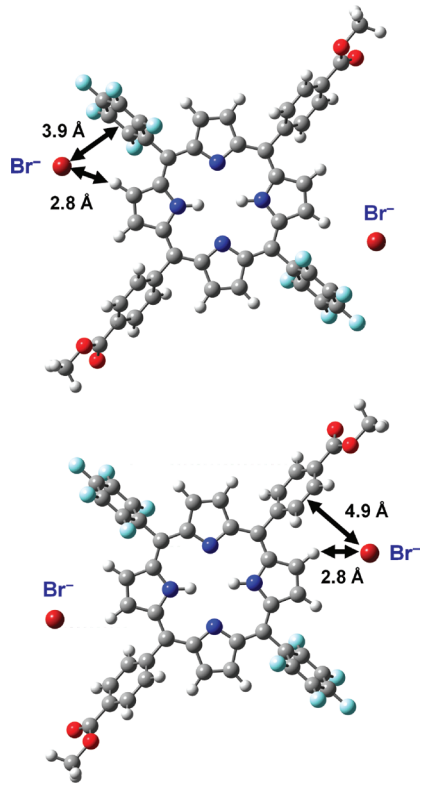

Figure 7. Bromide binding sites of the bispentafluorophenyl free-base porphyrin sensitizer bearing linkers for attachment to metal-oxide surfaces: (top) two equivalent low-energy positions at 3.9 Å from the pentafluorophenyl groups, stabilized by π−anion interactions with a stabilization energy of −7.9 kcal/mol, and (bottom) two similar positions at 4.9 Å from the carbomethoxyphenyl groups stabilized by −4.9 kcal/mol.

results in a larger barrier for back transfer of electrons from the semiconductor to the donor state and a favorable reduction in J_0 (see Scheme 3). The resulting reduction of the recombination current density J_0 reduces the slope of the characteristic curve at $V \rightarrow 0$ and increases the open circuit voltage V_{OC} (see Figures 4 and 5). The illumination current density increases (or decreases) when the donor state is displaced to a range of the conduction band with larger (or smaller) density of states relative to I_3^-/I^- depending on the energy level alignment of the donor state with the metal-oxide density of states.

DISCUSSION

Natural photosynthesis offers many desirable features; yet, not every facet should be a target for chemical mimicry. Biological photosynthetic machinery appears to be limited by the inherited "legacy" biochemistry of the quinone/quinol redox couple and key energy carriers such as NAD(P)H and ATP. The ability to alter the energetics of the primary electron acceptor, and other components, is a promising feature of artificial systems. Using anode materials with conduction-band energies poised more positive of TiO_2 (illustrated in this work by replacing TiO_2 with SnO_2) allows the energetics of a sensitizer dye to be tuned to higher potentials without adversely affecting the excited-state electron-transfer chemistry. Using this strategy, absorption of photons over a larger spectral range could be accomplished if photosystems were stacked in optical, in addition to electrical, series.[68,69] Unlike the natural photosynthetic apparatus, such an artificial Z-scheme (tandem cell)

dx.doi.org/10.1021/jp210096m | J. Phys. Chem. C 2012, 116, 4892−4902

Table 3. Ion−Ring Distances, Nearest Pyrrole H Distances, and Stabilization Energy E_s for One or Two Br^- Ions Bound to the Pentafluorophenyl or Carbomethoxyphenyl Rings of Sensitizers 1−3 Based on B3LYP/6-31G(d,p) Calculations[a]

		pentafluorophenyl rings			carbomethoxyphenyl rings		
		ion−ring	ion−H	E_s	ion−ring	ion−H	E_s
dye	number of ions	(Å)	(Å)	(kcal mol^{-1})	(Å)	(Å)	(kcal mol^{-1})
1	1	3.8	2.7	−4.5	4.9	2.9	−3.1
	2	3.9	2.8	−7.9	4.9	2.8	−4.9
2	1	4.3	2.9	−1.7	4.8	3.0	−1.1
	2	4.2	2.9	−2.6	4.8	3.0	−1.1
3	1	4.2	2.9	−2.3	4.8	3.0	−1.6
	2	4.2	2.9	−3.6	4.8	3.0	−2.0

[a]Two ions are bound to opposing rings as in Figure 7.

Scheme 3. Relative Shift in the Adsorbate Donor State to More Negative Potentials Due to a Reduction in the Concentration of Electrons at the Surface upon Substitution of I_3^-/I^- (Dashed Lines) with Br_3^-/Br^- (Solid Lines) in Solar Cells Based on 1, 2, or 3, Using TiO_2 or SnO_2 Nanocrystalline Substrates[a]

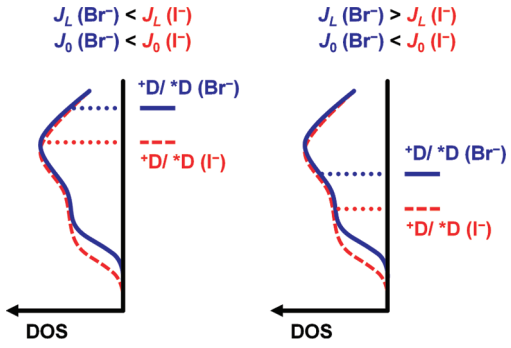

[a]In both cases, J_0 is reduced with bromide since the barrier for back transfer of electrons from the bottom of the metal-oxide conduction band to the donor state is increased. The illumination current density J_L is smaller (left panel) or larger (right panel) in Br_3^-/Br^-.

would provide a superior match to the solar spectrum while supplying the potentials required for the oxidative (water oxidation at an anode) and reductive (fuel formation at a cathode) half reactions.

CONCLUSIONS

We have prepared a selection of bioinspired, photochemically active constructs composed of high-potential porphyrin dyes attached to TiO_2 and SnO_2 nanoparticle metal-oxide surfaces. This strategy allows us to tune the optical and electronic properties of the individual system components to provide highly oxidizing conditions. Using DSSCs as a platform for evaluating the energetics of dye/metal oxide interfaces and a tool to screen for systems capable of oxidizing relatively high-potential electron sources, we show the ability of our freebase and palladium porphyrin anodes to use the Br_3^-/Br^- redox couple as a regenerative electron mediator. These results are in stark contrast to those obtained for systems utilizing lower-potential sensitizers such as the Ru-polypyridyl-based dye N719, where the iodide relay alone gives optimal results. Further, we find that our free-base (**1**) and palladium (**3**) porphyrin sensitizers immobilized on SnO_2-based nanocrystalline photoelectrochemical cells (PECs) yield a higher overall energy conversion efficiency (η) with the Br_3^-/Br^- redox couple over the lower-potential I_3^-/I^- relay (a 660% and 1011% increase in η, respectively). However, the best overall solar-to-electric conversion efficiency of the devices studied here (η = 1%) is significantly lower than those reported for the most highly optimized DSSCs ($\eta \sim 11\%$) which utilize the lower-potential I_3^-/I^- couple. Our computational modeling of the structures and equivalent circuits assists in a molecular-based understanding of these results. In conclusion, the potentials photogenerated at the porphyrin-sensitized anode surface are favorably poised for water oxidation; thus, they are relevant for solar-to-fuel applications in artificial photosynthesis. Future work will focus on interfacing these high-potential photoanodes with water-oxidation catalysts.

ASSOCIATED CONTENT

Supporting Information

Synthesis and Structural Characterization, Optical Data, Electrochemical Data, Computational Data, and complete reference 49. This material is available free of charge via the Internet at http://pubs.acs.org.

AUTHOR INFORMATION

Corresponding Author

*E-mail: minjoo.lee@yale.edu; victor.batista@yale.edu; charles.schmuttenmaer@yale.edu; robert.crabtree@yale.edu; gary.brudvig@yale.edu.

Present Address

[§]Joint Center for Artificial Photosynthesis, Lawrence Berkeley National Laboratory, Berkeley, CA 94720.

Notes

The authors declare no competing financial interest.

ACKNOWLEDGMENTS

This work was supported by the Office of Basic Energy Sciences of the U.S. Department of Energy (DE-FG02-07ER15909) and the Camille & Henry Dreyfus Foundation.

REFERENCES

(1) *New Sciences for a Secure and Sustainable Energy Future*; U.S. Dept. of Energy: Washington, D. C., December, 2008.
(2) *IPCC, 2007: Summary for policy makers*; Cambridge University Press: U.K., 2007.
(3) Hoffert, M. I.; Caldeira, K.; Jain, A. K.; Haites, E. F.; Harvey, L. D. D.; Potter, S. D.; Schlesinger, M. E.; Schneider, S. H.; Watts, R. G.; Wigley, T. M. L.; Wuebbles, D. J. *Nature* **1998**, *395*, 881−884.
(4) Lewis, N. S.; Nocera, D. G. *Proc. Natl. Acad. Sci.* **2006**, *103*, 15729−15735.
(5) *International energy outlook 2009*; U.S. Dept. of Energy: Washington, D. C., May, 2009.

(6) *Directing Matter and Energy: Five Challenges for Science and the Imagination*; U.S. Dept. of Energy: Washington, D. C., December, 2007.
(7) *Basic Research Needs: Catalysis For Energy*; U.S. Dept. of Energy: Washington, D. C., August, 2007.
(8) McEvoy, J. P.; Brudvig, G. W. *Chem. Rev.* **2006**, *106*, 4455−4483.
(9) Barber, J. *Chem. Soc. Rev.* **2009**, *38*, 185−196.
(10) Moore, G. F.; Brudvig, G. W. *Annu. Rev. Condens. Matter Phys.* **2011**, *2*, 303−327.
(11) Wasielewski, M. R. *Chem. Rev.* **1992**, *92*, 435−461.
(12) Gust, D.; Moore, T. A.; Moore, A. L. *Acc. Chem. Res.* **1993**, *26*, 198−205.
(13) Gust, D.; Moore, T. A.; Moore, A. L. *Acc. Chem. Res.* **2001**, *34*, 40−48.
(14) Gust, D.; Kramer, D.; Moore, A.; Moore, T. A.; Vermaas, W. *MRS Bull.* **2008**, *33*, 383−387.
(15) Gust, D.; Moore, T. A.; Moore, A. L. *Acc. Chem. Res.* **2009**, *42*, 1890−1898.
(16) Hambourger, M.; Moore, G. F.; Kramer, D. M.; Gust, D.; Moore, A. L.; Moore, T. A. *Chem. Soc. Rev.* **2009**, *38*, 25−35.
(17) Fukuzumi, S. *Phys. Chem. Chem. Phys.* **2008**, *10*, 2283−2297.
(18) Hammarström, L. *Curr. Opin. Chem. Biol.* **2003**, *7*, 666−673.
(19) O'Regan, B.; Grätzel, M. *Nature* **1991**, *353*, 737−740.
(20) Grätzel, M. *Nature* **2001**, *414*, 338−344.
(21) Ardo, S.; Meyer, G. J. *Chem. Soc. Rev.* **2009**, *38*, 115−164.
(22) Campbell, W. M.; Burrell, A. K.; Officer, D. L.; Jolley, K. W. *Coord. Chem. Rev.* **2004**, *248*, 1363−1379.
(23) Dabestani, R.; Bard, A. J.; Campion, A.; Fox, M. A.; Mallouk, T. E.; Webber, S. E.; White, J. M. *J. Phys. Chem.* **1988**, *92*, 1872−1878.
(24) Hasselman, G. M.; Watson, D. F.; Stromberg, J. R.; Bocian, D. F.; Holten, D.; Lindsey, J. S.; Meyer, G. J. *J. Phys. Chem. B* **2006**, *110*, 25430−25440.
(25) Morris, A. J.; Marton, A.; Meyer, G. J. *Inorg. Chem.* **2008**, *47*, 7681−7685.
(26) Lu, H.-P.; Mai, C.-L.; Tsia, C.-Y.; Hsu, S.-J.; Hsieh, C.-P.; Chiu, C.-L.; Yeh, C.-Y.; Diau, E. W.-G. *Phys. Chem. Chem. Phys.* **2009**, *11*, 10270−10274.
(27) Ooyama, Y.; Harima, Y. *Eur. J. Org. Chem.* **2009**, 2903−2934.
(28) Radivojevic, I.; Varotto, A.; Farley, C.; Drain, C. M. *Energy Environ. Sci.* **2010**, *3*, 1897−1909.
(29) Ning, Z.; Fu, Y.; Tian, H. *Energy Environ. Sci.* **2010**, *3*, 1170−1181.
(30) Boschloo, G.; Hagfeldt, A. *Acc. Chem. Res.* **2009**, *42*, 1819−1826.
(31) Fujishima, A.; Honda, K. *Nature* **1972**, *238*, 37−38.
(32) Youngblood, W. J.; Lee, S.-H. A.; Kobayashi, Y.; Hernandez-Pagan, E. A.; Hoertz, P. G.; Moore, T. A.; Moore, A. L.; Gust, D.; Mallouk, T. E. *J. Am. Chem. Soc.* **2009**, *131*, 926−927.
(33) Youngblood, W. J.; Lee, S.-H. A.; Maeda, K.; Mallouk, T. E. *Acc. Chem. Res.* **2009**, *42*, 1966−1973.
(34) Brimblecombe, R.; Koo, A.; Dismukes, G. C.; Swiegers, G. F.; Spiccia, L. *J. Am. Chem. Soc.* **2010**, *132*, 2892−2894.
(35) Marcus, R. A.; Sutin, N. *Biochim. Biophys. Acta, Bioenerg.* **1985**, *811*, 265−322.
(36) Blankenship, R. E. *Photosynth. Res.* **1992**, *33*, 91−111.
(37) Rutherford, A. W.; Faller, P. *Philos. Trans. R. Soc. London, Ser. B* **2003**, *358*, 245−253.
(38) Moore, G. F.; Blakemore, J. D.; Milot, R. L.; Hull, J. F.; Song, H.; Cai, L.; Schmuttenmaer, C. A.; Crabtree, R. H.; Brudvig, G. W. *Energy Environ. Sci.* **2011**, *4*, 2389−2392.
(39) Hagfeldt, A.; Boschloo, G.; Sun, L.; Kloo, L.; Pettersson, H. *Chem. Rev.* **2010**, *110*, 6595−6663.
(40) Hamann, T. W.; Jensen, R. A.; Martinson, A. B. F.; Van Ryswyk, H.; Hupp, J. T. *Energy Environ. Sci.* **2008**, *1*, 66−78.
(41) Vlachopoulos, N.; Liska, P.; Augustynski, J.; Grätzel, M. *J. Am. Chem. Soc.* **1988**, *110*, 1216−1220.
(42) Hara, K.; Horiguchi, T.; Kinoshita, T.; Sayama, K.; Arakawa, H. *Sol. Energy Mater. Sol. Cells* **2001**, *70*, 151−161.
(43) Ferrere, S.; Zaban, A.; Gregg, B. A. *J. Phys. Chem. B* **1997**, *101*, 4490−4493.
(44) Wang, Z.-S.; Sayama, K.; Sugihara, H. *J. Phys. Chem. B* **2005**, *109*, 22449−22455.
(45) Suri, P.; Mehra, R. M. *Sol. Energy Mater. Sol. Cells* **2007**, *91*, 518−524.
(46) Beard, M. C.; Turner, G. M.; Schmuttenmaer, C. A. *Phys. Rev. B: Condens. Matter Mater. Phys.* **2000**, *62*, 15764−15777.
(47) Baxter, J. B.; Schmuttenmaer, C. A. *J. Phys. Chem. B* **2006**, *110*, 25229−25239.
(48) Turner, G. M.; Beard, M. C.; Schmuttenmaer, C. A. *J. Phys. Chem. B* **2002**, *106*, 11716−11721.
(49) Frisch, M. J.; Trucks, G. W.; Schlegel, H. B.; Scuseria, G. E.; Robb, M. A.; Cheeseman, J. R.; Scalmani, G.; Barone, V.; Mennucci, B.; Petersson, G. A.; Nakatsuji, H.; et al. Gaussian 09, Revision A.1; D. J. Gaussian, Inc.: Wallingford CT, 2009.
(50) Singh, U. C.; Kollman, P. A. *J. Comput. Chem.* **1984**, *5*, 129−145.
(51) Besler, B. H.; Merz, K. M. Jr.; Kollman, P. A. *J. Comput. Chem.* **1990**, *11*, 431−439.
(52) El Guibaly, F.; Colbow, K. *Can. J. Phys.* **1981**, *59*, 1682−1685.
(53) El Guibaly, F.; Colbow, K.; Funt, B. L. *J. Appl. Phys.* **1981**, *52*, 3480−3483.
(54) Moore, G. F.; Hambourger, M.; Gervaldo, M.; Poluektov, O. G.; Rajh, T.; Gust, D.; Moore, T. A.; Moore, A. L. *J. Am. Chem. Soc.* **2008**, *130*, 10466−10467.
(55) Moore, G. F.; Hambourger, M.; Kodis, G.; Michl, W.; Gust, D.; Moore, T. A.; Moore, A. L. *J. Phys. Chem. B* **2010**, *114*, 14450−14457.
(56) Rehm, D.; Weller, A. *Ber. Bunsenges. Phys. Chem.* **1969**, *73*, 834−839.
(57) Rehm, D.; Weller, A. *Isr. J. Chem.* **1970**, *8*, 259−271.
(58) Rothenberger, G.; Fitzmaurice, D.; Grätzel, M. *J. Phys. Chem.* **1992**, *96*, 5983−5986.
(59) Nazeeruddin, M. K.; Kay, A.; Rodicio, I.; Humphry-Baker, R.; Mueller, E.; Liska, P.; Vlachopoulos, N.; Grätzel, M. *J. Am. Chem. Soc.* **1993**, *115*, 6382−6390.
(60) Huang, S. Y.; Schlichthoerl, G.; Nozik, A. J.; Grätzel, M.; Frank, A. J. *J. Phys. Chem. B* **1997**, *101*, 2576−2582.
(61) Kumar, A.; Santangelo, P. G.; Lewis, N. S. *J. Phys. Chem.* **1992**, *96*, 834−839.
(62) Ai, X.; Anderson, N. A.; Guo, J.; Lian, T. *J. Phys. Chem. B* **2005**, *109*, 7088−7094.
(63) Benko, G.; Myllyperkio, P.; Pan, J.; Yartsev, A. P.; Sundström, V. *J. Am. Chem. Soc.* **2003**, *125*, 1118−1119.
(64) Myllyperkio, P.; Benko, G.; Korppi-Tommola, J.; Yartsev, A. P.; Sundström, V. *Phys. Chem. Chem. Phys.* **2008**, *10*, 996−1002.
(65) Furube, A.; Murai, M.; Watanabe, S.; Hara, K.; Katoh, R.; Tachiya, M. *J. Photochem. Photobiol. A* **2006**, *182*, 273−279.
(66) Garau, C.; Frontera, A.; Quinonero, D.; Ballester, P.; Costa, A.; Deya, P. M. *Chem. Phys. Chem.* **2003**, *4*, 1344−1348.
(67) Garau, C.; Frontera, A.; Quiñonero, D.; Ballester, P.; Costa, A.; Deyà, P. *J. Phys. Chem. A* **2004**, *108*, 9423−9427.
(68) Shockley, W.; Queisser, H. J. *J. Appl. Phys.* **1961**, 510−519.
(69) Hanna, M. C.; Nozik, A. J. *J. Appl. Phys.* **2006**, *100*, 074510/1−074510/8.

Supporting Information for

Bioinspired High-Potential Porphyrin Photoanodes

Gary F. Moore,[a] *Steven J. Konezny,*[a] *Hee-eun Song,*[a] *Rebecca L. Milot,*[a] *James D. Blakemore,*[a] *Minjoo L. Lee,*[b,*] *Victor S. Batista,*[a,*] *Charles A. Schmuttenmaer,*[a,*] *Robert H. Crabtree,*[a,*] *and Gary W. Brudvig*[a,*]

[a] Department of Chemistry, Yale University, P.O. Box 208107, New Haven, Connecticut 06520-8107; and [b] Yale School of Engineering and Applied Science, Yale University, P.O. Box 208267, New Haven Connecticut 06520-8267

minjoo.lee@yale.edu, charles.schmuttenmaer@yale.edu, victor.batista@yale.edu, robert.crabtree@yale.edu, gary.brudvig@yale.edu

Index ***Page***

Synthesis and Structural Characterization

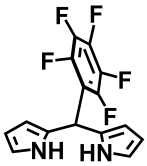

5-(Pentafluorophenyl)dipyrromethane. A similar method was previously reported.[S1] A solution of pentafluorobenzaldehyde (2.0 mL, 16.2 mmol) in freshly distilled pyrrole (50 mL, 720 mmol) was degassed with a stream of argon for 20 min before adding trifluoroacetic acid (120 μL, 1.62 mmol). The mixture was stirred for 30 min at room temperature, diluted with CH_2Cl_2 (400 mL), and then washed with 0.1M NaOH (400 mL). The organic phase was washed with water (400 mL) and dried over Na_2SO_4. Evaporation of the solvent at reduced pressure gave brown oil. Unreacted pyrrole was removed under high vacuum, yielding a tacky solid that was flashed on a column of silica using a mixture of hexanes:ethyl acetate:triethylamine (80:20:1) as the eluent. The product was recrystallized from dichloromethane/hexanes to yield 3.29 g of 5-(pentafluorophenyl)dipyrromethane as a white powder (65% yield). ^{1}H NMR (400 MHz, $CDCl_3$): δ 5.90 (1H, s, CH), 6.00 – 6.05 (2H, m, ArH), 6.14 – 6.19 (2H, m, ArH), 6.71 – 6.75 (2H, m, ArH), 8.06 (2H, brs, NH); ^{19}F NMR (400 MHz, $CDCl_3$): δ -160.98 – -161.40 (2F, m, ArF), -155.71 (1F, t, J = 21.0 Hz, ArF),) -141.43 (2F, brd, J = 20.7 Hz, ArF).

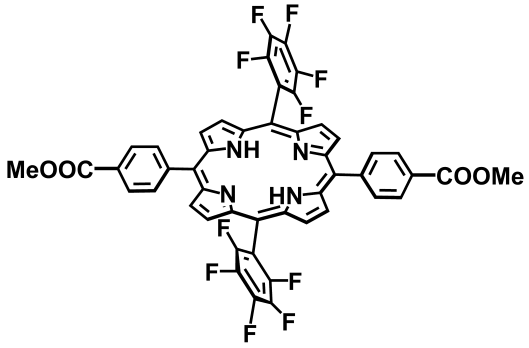

5,15-*Bis*(4-carbomethoxyphenyl)-10,20-*bis*(pentafluorophenyl)porphyrin. A portion of 5-(pentafluorophenyl)dipyrromethane (1.15 g, 3.68 mmol), and 4-carbomethoxybenzaldehyde (663 mg, 3.68 mmol) in chloroform (370 mL) was purged for 20 minutes with argon before adding $BF_3(OEt_2)$ (486 μL of a 2.5M stock solution in chloroform). After 24 h, 2,3-dichloro-5,6-dicyano-1,4-benzoquinone (DDQ) (625 mg, 2.75 mmol) was added and the mixture was stirred for an additional 24 h. The solvent was evaporated at reduced pressure and the residue was redissolved in toluene. The solution was treated with a second portion of DDQ (625 mg, 2.75 mmol) and refluxed for 2.5 h. The toluene was removed at reduced pressure and the crude product was purified by column chromatography on silica using chloroform as the eluent.

Recrystallization from chloroform/methanol gave 318 mg of the desired porphyrin as a purple crystalline solid (19% yield). ^{1}H NMR (400 MHz, $CDCl_3$): δ -2.86 (2H, s, NH), 4.13 (6H, s, CO_2CH_3), 8.31 (4H, d, J = 8.1 Hz, ArH), 8.47 (4H, d, J= 8.1 Hz, ArH), 8.83 (4H, d, J= 4.8Hz, βH), 8.91 (4H, d, J= 4.8Hz, βH); ^{19}F NMR (400 MHz, in $CDCl_3$): δ -161.96 – -161.49 (4F, m, ArF), -151.95 (2F, t, J= 21.2 Hz, ArF); -136.81 (4F, dd, J= 8.1 Hz, 23.7 Hz, ArF); MALDI-TOF-MS *m/z.* calcd. for $C_{48}H_{24}F_{10}N_4O_4$ 910.164, obsd. 910.169; UV-vis (CH_2Cl_2) 416, 510, 543 587, 641 nm. Emission (CH_2Cl_2) 646, 709 nm.

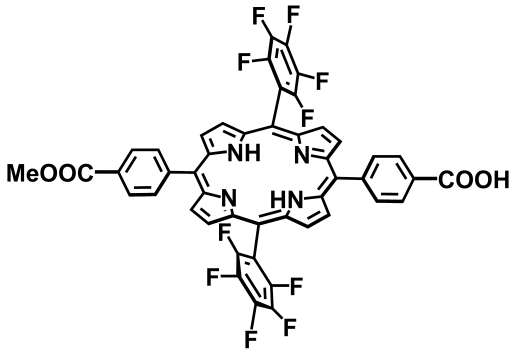

5-(4-Carbomethoxyphenyl)-15-(4-carboxyphenyl)-10,20-*bis*(pentafluorophenyl)porphyrin (1). A portion of 5,15-*bis*(4-carbomethoxyphenyl)-10,20-*bis*(pentafluorophenyl)porphyrin (100 mg, 0.11 mmol) was dissolved in a mixture of trifluoroacetic acid and conc. HCl (1:2, 80 mL) at 45^o C for 24 h. The reaction mixture was diluted with dichloromethane (80 mL), washed twice with an equal volume of water, and then neutralized with a saturated solution of aqueous sodium bicarbonate. The organic phase was dried over sodium sulfate, filtered, and the solvent removed at reduced pressure. The crude product was purified by column chromatography on silica using a gradient of 1% methanol in dichloromethane to 10% methanol in dichloromethane as the eluent to give 59 mg of the desired porphyrin (60% yield). ^{1}H NMR (500 MHz, 1% Pyridine-*d*5 in $CDCl_3$): δ -2.86 (2H, s, NH), 4.11 (3H, s, CO_2CH_3), 8.30 (2H, d, J = 8.4 Hz, ArH), 8.31 (2H, d, J = 8.4 Hz, ArH), 8.48 (2H, d, J= 8.2 Hz, ArH), 8.59 (2H, d, J= 8.2 Hz, ArH), 8.87 (4H, brm, βH), 8.91 (2H, d, J= 4.8 Hz, βH), 8.96 (2H, d, J= 4.8 Hz, βH); ^{19}F NMR (400 MHz, 1% Pyridine-*d*5 in $CDCl_3$): δ -161.96 – -161.78 (4F, m, ArF), -152.16 (2F, t, J = 21.0 ArF), -137.03 (4F, dd, J = 8.0 Hz, 23.9 Hz, ArF); MALDI-TOF-MS *m/z.* calcd. for $C_{47}H_{22}F_{10}N_4O_4$ 896.148, obsd. 896.153.

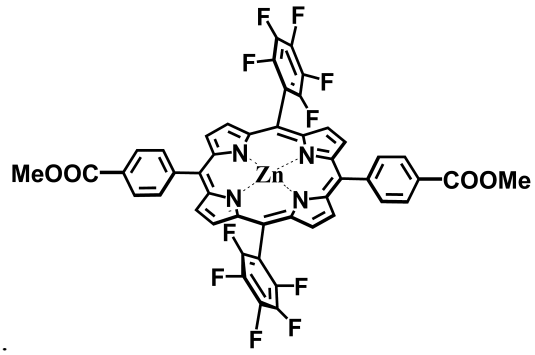

Zinc 5,15-*bis*(4-carbomethoxyphenyl)-10,20-*bis*(pentafluorophenyl)porphyrin. $Zn(OAc_2)\cdot 2H_2O$ (84 mg, 0.38 mmol) was added to a solution of 5,15-*bis*(4-carbomethoxyphenyl)-10,20-*bis*(pentafluorophenyl)porphyrin (35 mg, 0.04 mmol) in a mixture

of dichloromethane and methanol (80:20, 50 mL). After stirring for 15 h, the solution was diluted with dichloromethane (25 mL) and washed with water (75 mL), then a saturated solution of aqueous sodium bicarbonate. The organic phase was dried over sodium sulfate, filtered, and the solvent evaporated at reduced pressure. The product was purified by column chromatography on silica using dichloromethane as the eluent to give 37 mg of the desired porphyrin (98% yield). ^{1}H NMR (500 MHz, 1% Pyridine-*d*5 in $CDCl_3$): δ 4.09 (6H, s, CO_2CH_3), 8.24 (4H, d, J = 8.3 Hz, ArH), 8.42 (4H, d, J = 8.3 Hz, ArH), 8.87 (4H, d, J = 4.8Hz, βH), 8.90 (4H, d, J = 4.8Hz, βH); ^{19}F NMR (400 MHz, 1% Pyridine-*d*5 in $CDCl_3$): δ -162.68 – -162.49 (4F, m, ArF), -153.29 (2F, t, J = 20.9 Hz, ArF); -137.54 (4F, dd, J = 8.5 Hz, 24.7 Hz, ArF); MALDI-TOF-MS *m/z*. calcd. for $C_{48}H_{22}F_{10}N_4O_4Zn$ 927.077, obsd. 927.079 UV-vis (CH_2Cl_2) 415, 545, 578 nm Emission (CH_2Cl_2) 590, 642 nm.

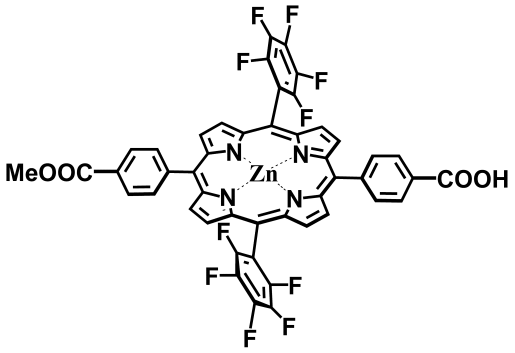

Zinc 5-(4-carbomethoxyphenyl)-15-(4-carboxyphenyl)-10,20-*bis*(pentafluorophenyl) porphyrin (2). $Zn(OAc_2)\cdot 2H_2O$ (98 mg, 0.45 mmol) was added to a solution of 5-(4-carbomethoxyphenyl)-15-(4-carboxyphenyl)-10,20-*bis*(pentafluorophenyl)porphyrin (40 mg, 0.04 mmol) in a mixture of dichloromethane and methanol (80:20, 60 mL). After stirring for 15 h, the solution was diluted with dichloromethane (25 mL) and washed with water (85 mL), then a saturated solution of aqueous sodium bicarbonate. The organic phase was dried over sodium sulfate, filtered, and the solvent evaporated at reduced pressure. The product was purified by column chromatography on silica using 5% methanol in dichloromethane as the eluent to give 42 mg of the desired porphyrin (97% yield). ^{1}H NMR (500 MHz, 1% Pyridine-*d*5 in $CDCl_3$): δ 4.10 (3H, s, CO_2CH_3), 8.24 (2H, d, J = 8.1 Hz, ArH), 8.25 (2H, d, J = 8.1 Hz, ArH), 8.42 (2H, d, J = 8.1 Hz, ArH), 8.52 (2H, d, J = 8.1 Hz, ArH), 8.87 (4H, brd, J = 4.6 Hz, βH), 8.90 (2H, d, J = 4.6 Hz, βH); 8.95 (2H, d, J = 4.6 Hz, βH); ^{19}F NMR (400 MHz, 1% Pyridine-*d*5 in $CDCl_3$): δ -162.76 – -162.51 (4F, m, ArF), -153.37 (2F, t, J = 21.1 Hz, ArF); -137.51 (4F, dd, J = 8.3 Hz, 24.5 Hz, ArF); MALDI-TOF-MS *m/z*. calcd. for $C_{47}H_{20}F_{10}N_4O_4Zn$ 958.062, obsd. 958.062.

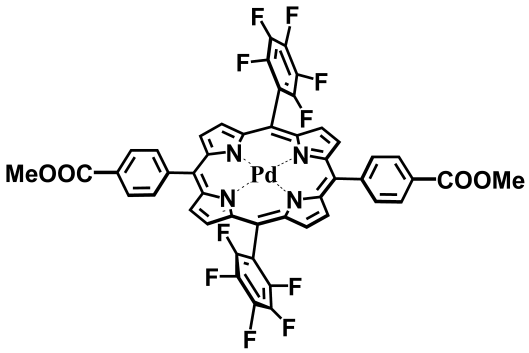

Palladium 5,15-*bis*(4-carbomethoxyphenyl)-10,20-*bis*(pentafluorophenyl)porphyrin. Palladium (II) chloride (67 mg, 0.38 mmol) was added to a solution of 5,15-*bis*(4-carbomethoxyphenyl)-10,20-*bis*(pentafluorophenyl)porphyrin (35 mg, 0.04 mmol) in N,N-dimethylformamide (15 mL). The mixture was stirred for 7h at reflux under an argon atmosphere. The solvent was removed under reduced pressure and the crude product was purified by column chromatography on silica using chloroform as the eluent. Recrystallization from chloroform/methanol gave 36 mg of the desired porphyrin as an orange crystalline solid (94% yield). ^{1}H NMR (500 MHz, $CDCl_3$): δ 4.12 (6H, s, CO_2CH_3), 8.27 (4H, d, J = 8.2 Hz, ArH), 8.46 (4H, d, J= 8.2 Hz, ArH), 8.79 (4H, d, J= 5.0 Hz, βH), 8.87 (4H, d, J= 5.0 Hz, βH); ^{19}F NMR (400 MHz, in $CDCl_3$): δ -161.72 – -161.50 (4F, m, ArF), -152.04 (2F, t, J= 20.7 Hz, ArF); -137.54 (4F, dd, J = 8.0 Hz, 25.2 Hz, ArF); MALDI-TOF-MS *m/z.* calcd. for $C_{48}H_{22}F_{10}N_4O_4Pd$ 1014.052, obsd. 1014.055 UV-vis (CH_2Cl_2) 412, 521, 554 nm. Emission (CH_2Cl_2) 560, 607 nm.

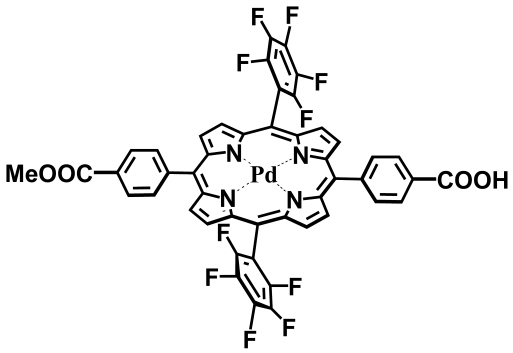

Palladium 5-(4carbomethoxyphenyl)-15-(4-carboxyphenyl)-10,20-*bis*(pentafluorophenyl) porphyrin (3). Palladium (II) chloride (78 mg, 0.45 mmol) was added to a solution of 5-(4-carbomethoxyphenyl)-15-(4-carboxyphenyl)-10,20-*bis*(pentafluorophenyl) porphyrin (40 mg, 0.04 mmol) in N,N-dimethylformamide(18 mL). The mixture was stirred for 7h at reflux under an argon atmosphere. The solvent was removed under reduced pressure and the crude product was purified by column chromatography on silica using 5% methanol in dichloromethane as the eluent. Recrystallization from chloroform/hexanes gave 42 mg of the desired porphyrin as an orange crystalline solid (93% yield). ^{1}H NMR (500 MHz, 1% Pyridine-*d*5 in $CDCl_3$): δ 4.11 (3H, s, CO_2CH_3), 8.26 (4H, brd, J = 8.2 Hz, ArH), 8.46 (2H, d, J = 8.2 Hz, ArH), 8.56 (2H, d, J= 8.2 Hz, ArH), 8.81 (4H, brd, J = 4.7 Hz, βH), 8.87 (2H, d, J = 4.7 Hz, βH); 8.93 (2H, d, J= 4.7 Hz, βH); ^{19}F NMR (400 MHz, 1% Pyridine-*d*5 in $CDCl_3$): δ -162.80 – -162.58 (4F, m, ArF), -152.04 (2F, t, J= 20.7 Hz, ArF); -136.86 (4F, dd, J= 8.0 Hz, 25.2 Hz, ArF); MALDI-TOF-MS *m/z.* calcd. for $C_{47}H_{20}F_{10}N_4O_4Pd$ 1000.036 obsd. 1000.040.

Optical Data

Figure S1. Absorption spectra of the methyl esters of (a) **1**, (b) **2**, and (c) **3** in dichloromethane.

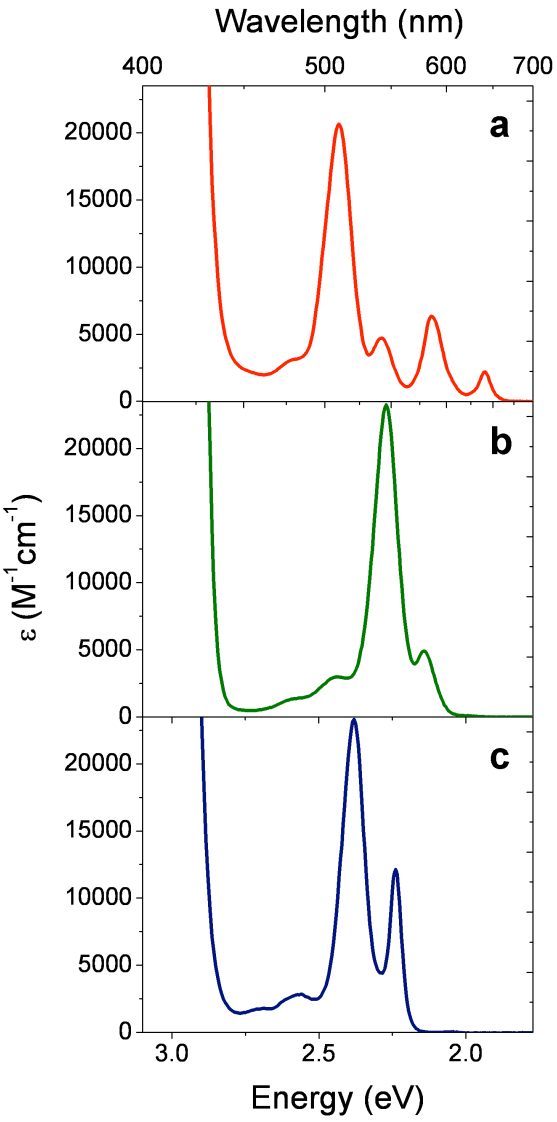

Figure S2. Absorption spectra, with a normalized O.D. of 1 at the Soret (dashed lines) and Q-band (solid lines) transitions, of the methyl esters of (a) **1**, (b) **2**, and (c) **3** in dichloromethane.

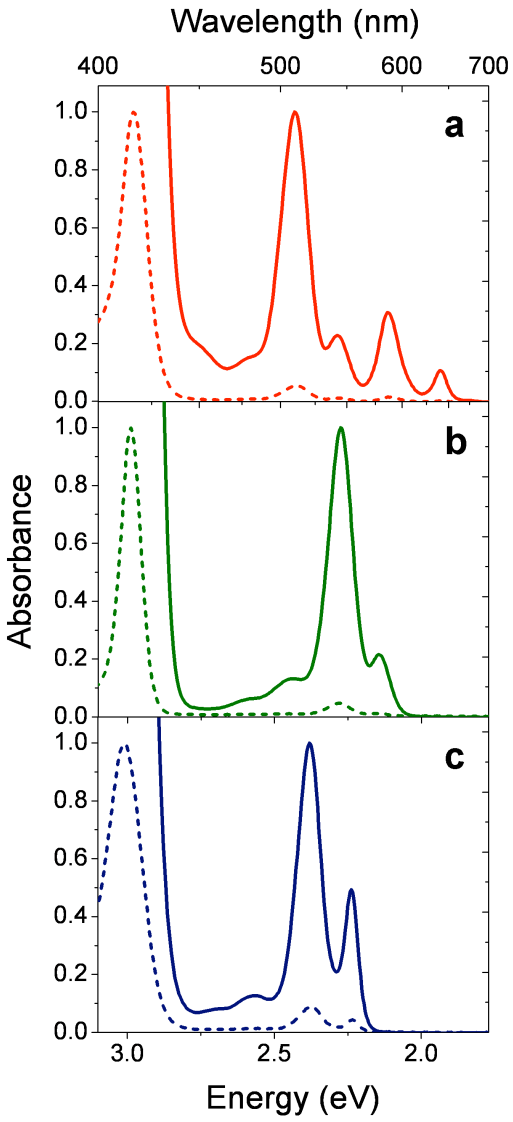

Figure S3. Absorption (solid lines) and emission (dashed lines) spectra, with a normalized relative intensity of 1 at the lowest energy absorption and highest energy emission bands, of the methyl esters of (a) **1**, (b) **2**, and (c) **3** in dichloromethane.

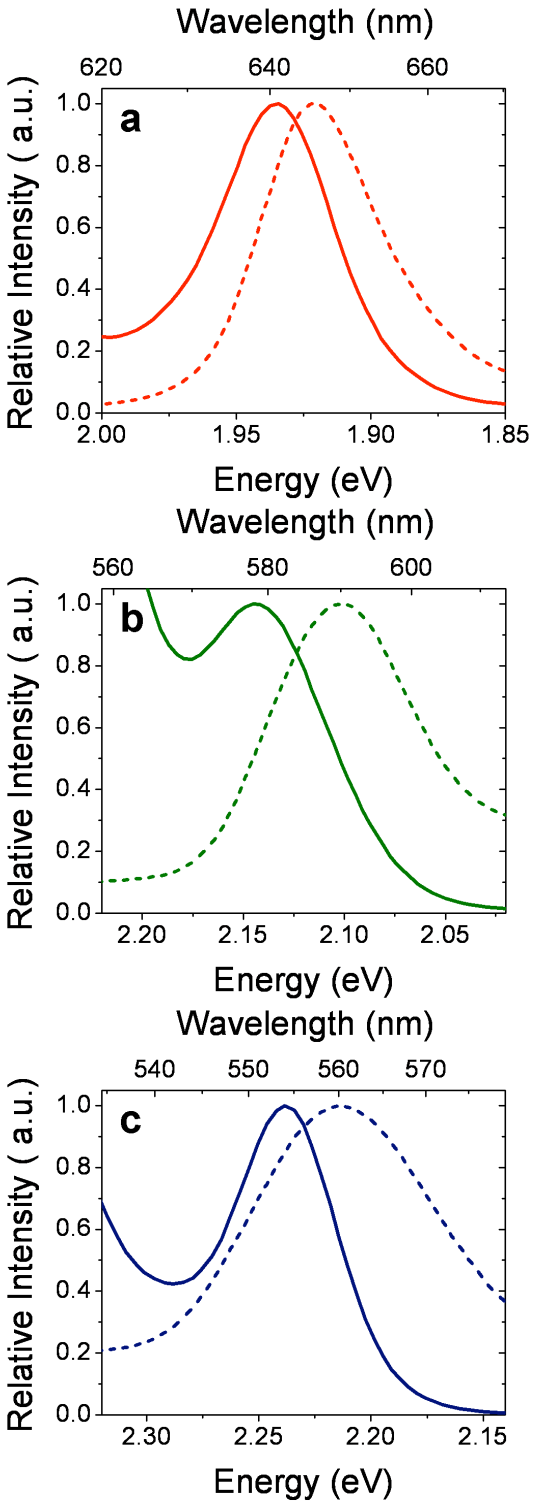

Figure S4. Diffuse reflectance spectra of (a) **1**, (b) **2**, and (c) **3** sensitized on mesoporous thin films of TiO_2 (solid lines) and SnO_2 (dashed lines).

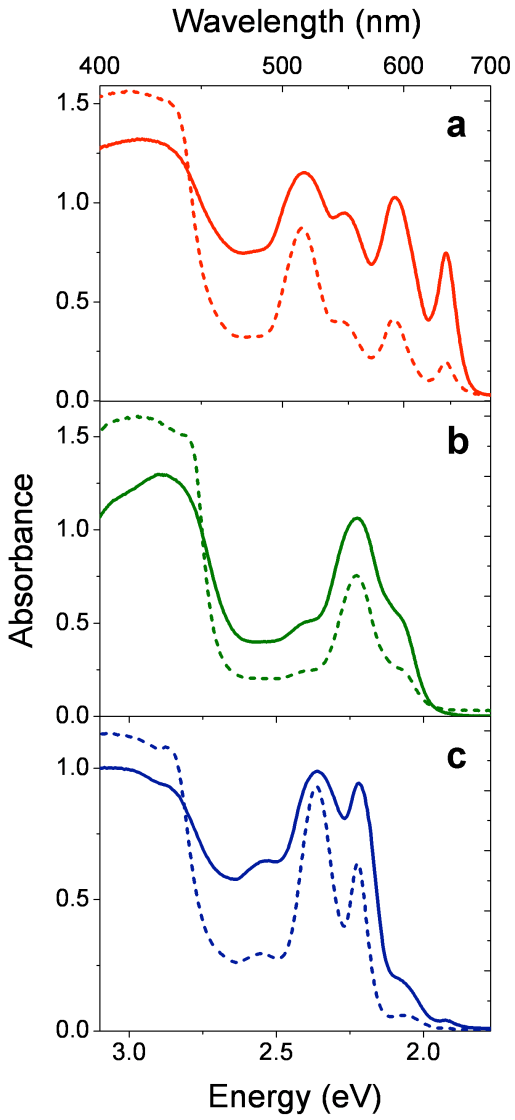

Figure S5. Photocurrent action spectra obtained with TiO_2 nanocrystalline photoelectrochemical cells sensitized with (a) **1**, (b) **2**, and (c) **3** using either the I_3^-/I^- (solid lines) or Br_3^-/Br^- (dashed lines) redox couple as a regenerative electron mediator.

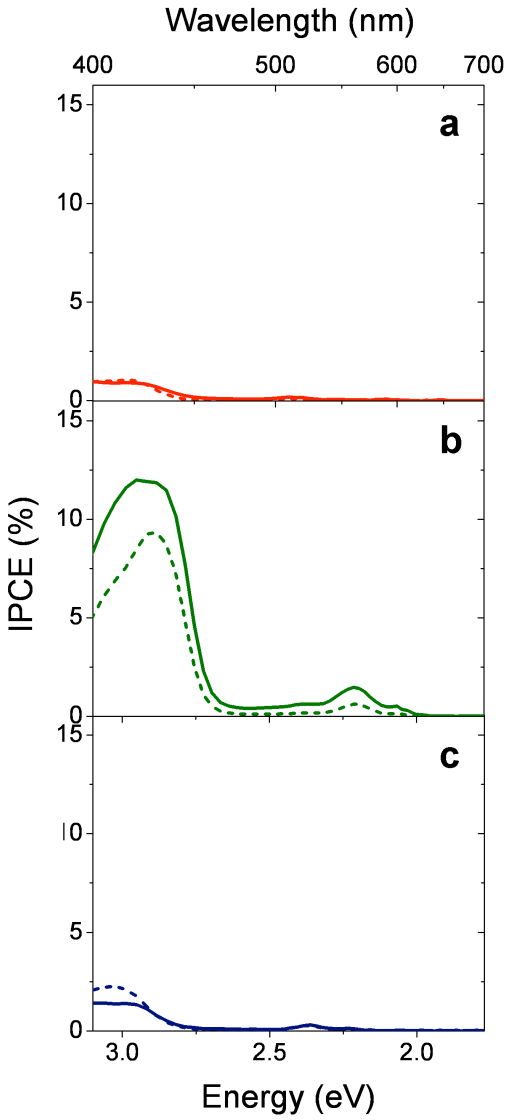

Figure S6. Photocurrent action spectra obtained with SnO_2 nanocrystalline photoelectrochemical cells sensitized with (a) **1**, (b) **2**, and (c) **3** using either the I_3^-/I^- (solid lines) or Br_3^-/Br^- (dashed lines) redox couple as a regenerative electron mediator.

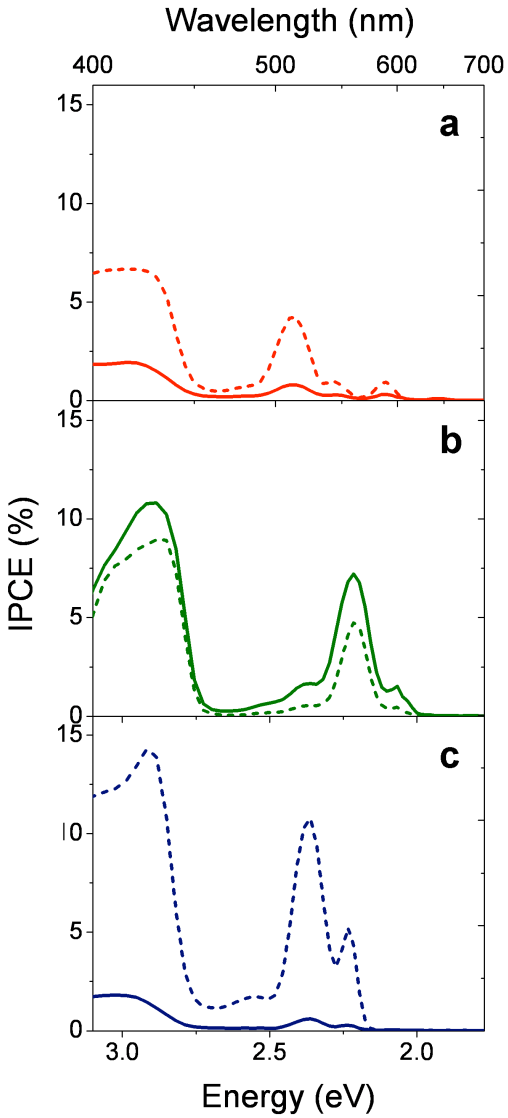

Electrochemical Data

Table S1. Measured redox potentials (E = $E_{1/2}$; quasi-reversible) for the methyl esters of **1–3** recorded in 0.10 M tetrabutylammonium hexafluorophosphate in dichloromethane (DCM).

Ester of Compound	Solvent	E (V vs. NHE)			
		^{II}E	^{I}E	^{i}E	^{ii}E
1	DCM	-1.11	-0.73	1.57	1.78
2	DCM	-1.33	-0.91	1.35	1.59
3	DCM	-1.29	-0.84	1.65	

Table S2. Estimated excited state redox potentials for the methyl esters of **1–3,** listed here and in the manuscript, were estimated from associated ground state redox potentials for the given couple and the $E^{0\text{-}0}$ transition energy for the light absorbing species using the following approximations:

$$E^{O}(P^{\bullet+} / {}^{1}P) \approx E^{O}(P^{\bullet+} / P) - \frac{E^{0-0}(P \rightarrow {}^{1}P)}{e}$$

$$E^{O}({}^{1}P / P^{\bullet-}) \approx E^{O}(P / P^{\bullet-}) + \frac{E^{0-0}(P \rightarrow {}^{1}P)}{e}$$

where $E^{O}(P^{\bullet+}/{}^{1}P)$ is the excited state redox potential for the porphyrin radical cation/excited singlet state porphyrin couple, $E^{O}(P^{\bullet+}/P)$ is the ground state potential for the porphyrin radical cation/porphyrin couple (taken as ^{i}E in Table S1), $E^{O}({}^{1}P/P^{\bullet-})$ is the excited state redox potential for the excited singlet state porphyrin/porphyrin radical anion couple, $E^{O}(P/P^{\bullet-})$ is the ground state potential for the porphyrin/porphyrin radical anion couple (taken as ^{I}E in Table S1), $E^{0\text{-}0}(P \rightarrow {}^{1}P)$ is the estimated $E^{0\text{-}0}$ porphyrin ground state to porphyrin excited singlet state transition energy determined from absorbance and fluorescence measurements (Figure S3) and *e* is the elementary charge of an electron.

Ester of Compound	Excited State E (V vs. NHE)	
	^{II}E	^{I}E
1	-0.36	1.20
2	-0.77	1.32
3	-0.58	1.39

Computational Data

Figure S7. Charge distributions and contour maps of the electrostatic potential surface for sensitizers **1-3**.

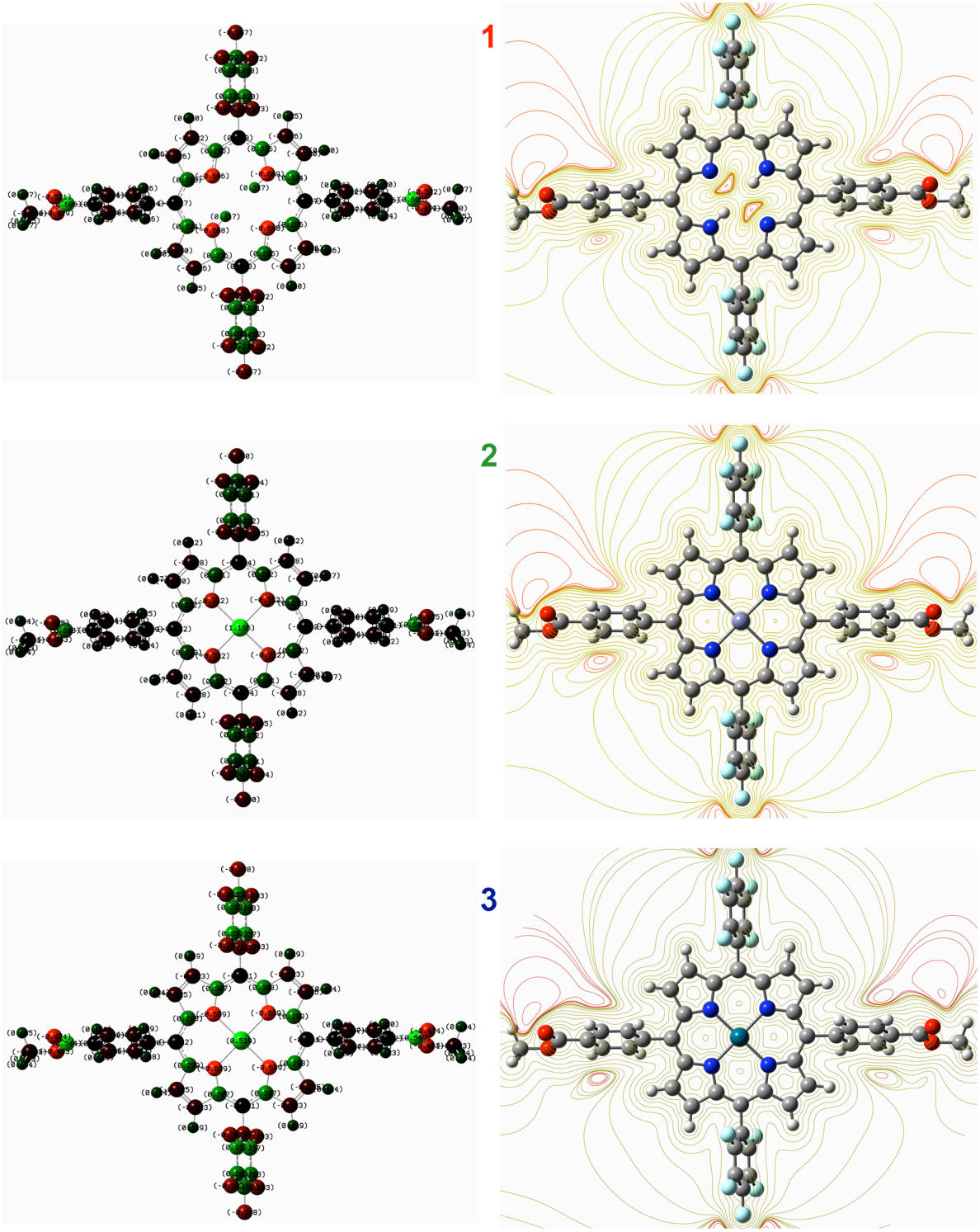

Complete Reference 49

(49) Frisch, M. J.; Trucks, G. W.; Schlegel, H. B.; Scuseria, G. E.; Robb, M. A.; Cheeseman, J. R.; Scalmani, G.; Barone, V.; Mennucci, B.; Petersson, G. A.; Nakatsuji, H.; Caricato, M.; Li, X.; Hratchian, H. P.; Izmaylov, A. F.; Bloino, J.; Zheng, G.; Sonnenberg, J. L.; Hada, M.; Ehara, M.; Toyota, K.; Fukuda, R.; Hasegawa, J.; Ishida, M.; Nakajima, T.; Honda, Y.; Kitao, O.; Nakai, H.; Vreven, T.; Montgomery, J., J. A. ; Peralta, J. E.; Ogliaro, F.; Bearpark, M.; Heyd, J. J.; Brothers, E.; Kudin, K. N.; Staroverov, V. N.; Kobayashi, R.; Normand, J.; Raghavachari, K.; Rendell, A.; Burant, J. C.; Iyengar, S. S.; Tomasi, J.; Cossi, M.; Rega, N.; Millam, J. M.; Klene, M.; Knox, J. E.; Cross, J. B.; Bakken, V.; Adamo, C.; Jaramillo, J.; Gomperts, R.; Stratmann, R. E.; Yazyev, O.; Austin, A. J.; Cammi, R.; Pomelli, C.; Ochterski, J. W.; Martin, R. L.; Morokuma, K.; Zakrzewski, V. G.; Voth, G. A.; Salvador, P.; Dannenberg, J. J.; Dapprich, S.; Daniels, A. D.; Farkas, Ö.; Foresman, J. B.; Ortiz, J. V.; Cioslowski, J.; Fox, D. J. Gaussian 09, Revision A.1; D. J. Gaussian, Inc.: Wallingford CT, 2009.